Supporting Information

Hierarchical Porous Carbon Nanofibers for Compatible Anode and Cathode of Potassium-Ion Hybrid Capacitor

Xiang Hu,[a,b+] Guobao Zhong,[a,b+] Junwei Li,[a+] Yangjie Liu,[a,b] Jun Yuan,[a] Junxiang Chen,[a] Hongbing Zhan,[b] Zhenhai Wen[a,*]

a CAS Key Laboratory of Design and Assembly of Functional Nanostructures, and Fujian Provincial Key Laboratory of Nanomaterials, Fujian Institute of Research on the Structure of Matter, Chinese Academy of Sciences, Fuzhou, Fujian 350002, China.

b College of Materials Science and Engineering, Fuzhou University, Fuzhou 350108, China

[+] These authors contributed equally to this work

* Corresponding authors

E-mail: wen@fjirsm.ac.cn

Experimental Section

Chemicals: Polyacrylonitrile (PAN, Mw = 150 000 g·mol^{-1}), 2-Methylimidazole ($C_4H_6N_2$, 2-MiM) and cetyltrimethylammonium bromide (CTAB) were all purchased from Sigma-Aldrich. Zinc acetate dihydrate ($Zn(CH_3COO)_2{\cdot}2H_2O$), triphenylphosphine (TPP), N,N-dimethylformamide (DMF), and urea (CH_4N_2O) were all purchased from Sinopharm Chemical Reagent Co., Ltd., China. All chemicals were of analytic grade and used without further purification.

Synthesis of ZIF-8 polyhedrons: Typically, 3 g of $Zn(CH_3COO)_2{\cdot}2H_2O$ was dissolved in 50 mL of water. 9.11 mg of CTAB and 11.165g of 2-MiM were dissolved in 50mL of water and stirred for 15 minutes to form a homogeneous solution. When the two solutions were rapidly mixed, the resulting suspension turned white after 20 s and aged for 3 h at room temperature. Next, the white powder was collected by centrifugation, washed with deionized water and dried at 70 ℃ for 12h.

Synthesis of PN-HPCNF: The PN-HPCNF nanofibers were synthesized by an electrospinning and subsequent carbonization process. First, 300 mg of TPP, 100 mg of CH_4N_2O and 500 mg of ZIF-8 were dissolved in 5 mL of DMF by sonication for 1 h, followed by the addition of 500 mg of PAN with vigorous stirring for 24 h to yield the homogeneously spinning solution. Then, the mixture solution was loaded into a syringe (5 mL) using a stainless-steel nozzle, which was connected to a high-voltage power supply. The parameters of electrospinning process, including voltage, collecting distance, and propel speed were set at 25 kV, 20 cm and 8 μL·min^{-1}, respectively. The obtained fibers were peeled off from the collector directly to the following thermal treatment process. Specifically, the PN-HPCNF nanofibers film was heated at a ramping rate 1 °C·min^{-1} to 250 °C, then kept for 5 h in air atmosphere. Afterwards, the nanofibers were carbonized at 500 °C for 1 h with a heating rate of 3 °C·min^{-1}, followed by further carbonization at 950 °C for 2 h with a heating rate of 5 °C·min^{-1} under Ar/H_2 (10%) atmosphere. Finally, a flexible phosphorus and nitrogen codoped hollow porous carbon

nanofibers (PN-HPCNF) film was obtained. As a comparison, nitrogen doped hollow porous carbon nanofibers (N-HPCNF) were prepared without the addition of TPP and nodoped hollow porous carbon nanofibers (HPCNF) were prepared without the addition of TPP and CH_4N_2O following the same thermal treatment conditions.

Materials characterization: Morphologies of samples were observed using field emission scanning electron microscopy (FESEM, Hitachi SU-8020), field emission transmission electron microscopy, and high-resolution transmission electron microscopy (FETEM, Tecnai F20). The disordered structure and defects were characterized by X-ray diffraction (XRD, Miniflex 600 powder X-ray diffractometer with a Cu Kα radiation source) and Raman spectrum (LabRam HR800). Nitrogen adsorption-desorption analysis were tested by an Intelligent Gravimetric Sorption Analyser (IGA100B). XPS analysis was performed using X-ray photoelectron spectroscopy (XPS, ESCALAB 250Xi, Thermo Fisher). The PN-HPCNF electrodes were disassembled at different stages in argon-filled glovebox, followed by washing the electrodes with diglyme to Ex-situ Raman, XRD, XPS, TEM and SEM measurements.

Electrochemistry characterization: The flexible and binder-free PN-HPCNF film was cut into small disks with diameter of 12 mm and directly used as electrodes. The average mass loading of whole electrode is about 0.8-1.0 mg cm^{-2}. The 2032 coin-type cells were assembled using the as-prepared films as the working electrode, potassium foil as the counter electrode and Whatman glass fibers as separator in an argon-filled glovebox (< 0.01 ppm of oxygen and water). The electrolyte was 1 M potassium bis(fluorosulfonyl)imide (KFSI) in diglyme. Galvanostatic charge-discharge tests were carried out in the potential range of 0.01-3.0V (vs K/K^+) at room temperature by a LAND CT2001 battery tester (Wuhan, China). The Cyclic voltammetry curves (0.1 mV s^{-1}, 0.01-3.0 V) and electrochemical impedance spectroscopy (0.01 Hz to 100 kHz) were recorded by a CHI660E electrochemical workstation.

A PIHCs full cell was assembled using the prepotassiation PN-HPCNF anode and APN-HPCNF cathode with a mass ratio ranging from of 1:2 to 1:4. The cathode was fabricated by

mixing the APN-HPCNF power, acetylene black, and poly(vinyl difluoride) in N-methyl pyrrolidone at 80:10:10 mass ratio and then casting the slurry on pure Al foil. Before the assembling of the full APN-HPCNF//PN-HPCNF PIHCs device, the anode was activated in half cell under 0.2 A g^{-1} for 5 cycles and ended with a potassiation state of 0.01 V. Finally, all specific capacities and current densities were based on the total mass of both anode and cathode materials in the PIHCs full-cell tests. The energy (E, Wh kg^{-1}) and power densities (P, W kg^{-1}) of the PIHCs full-cells were determined using the following equations:

$$P = \Delta V \times i \qquad \text{(Equation S1)}$$

$$E = P \times t/3600 \qquad \text{(Equation S2)}$$

$$\Delta V = (V_{max} + V_{min})/2 \qquad \text{(Equation S3)}$$

where t is the discharge time (s), i is the charge/discharge current (A g^{-1}), V_{max} is the potential at the beginning of discharge after the IR drop and V_{min} is the potential at the end of discharge voltages (V).

Calculation Method: DFT calculations were performed with periodic super-cells under the generalized gradient approximation (GGA) using the Perdew-Burke-Ernzerhof (PBE) function for exchange-correlation and the ultrasoft pseudopotentials for nuclei and core electrons. The Kohn-Sham orbitals were expanded in a plane-wave basis set with a kinetic energy cutoff of 30 Ry and the charge-density cutoff of 300 Ry. The adsorption energy ΔE_a can be calculated by the following equation:

$$\Delta E_a = E_{tot} - E_K - E_{str} \qquad \text{(Equation S4)}$$

where E_{tot} is the total energy of compound obtained from DFT calculations, E_K is the energy of K atoms and E_{str} is the energy of each structure. Electron density difference was calculated by subtracting the charge densities of K atoms and each configuration from the corresponding compounds. The Fermi-surface effects has been treated by the smearing technique of Methfessel and Paxton, using a smearing parameter of 0.02 Ry. The Brillouin-zones were

sampled with a k-point mesh of 3×3×1. The calculation model of the PN-HPCNF, N-HPCNF and HPCNF were constructed with 5×5 lateral periodicity shown in Figure S25-S27. The nudged elastic band (NEB) method was used to estimate the transition state and activation energy for a K atom to migrate from one hollow site of graphene in the PN-HPCNF, N-HPCNF and HPCNF to another hollow site. All the DFT calculations are implemented by the PW and NEB modules contained in the Quantum ESPRESSO distribution.

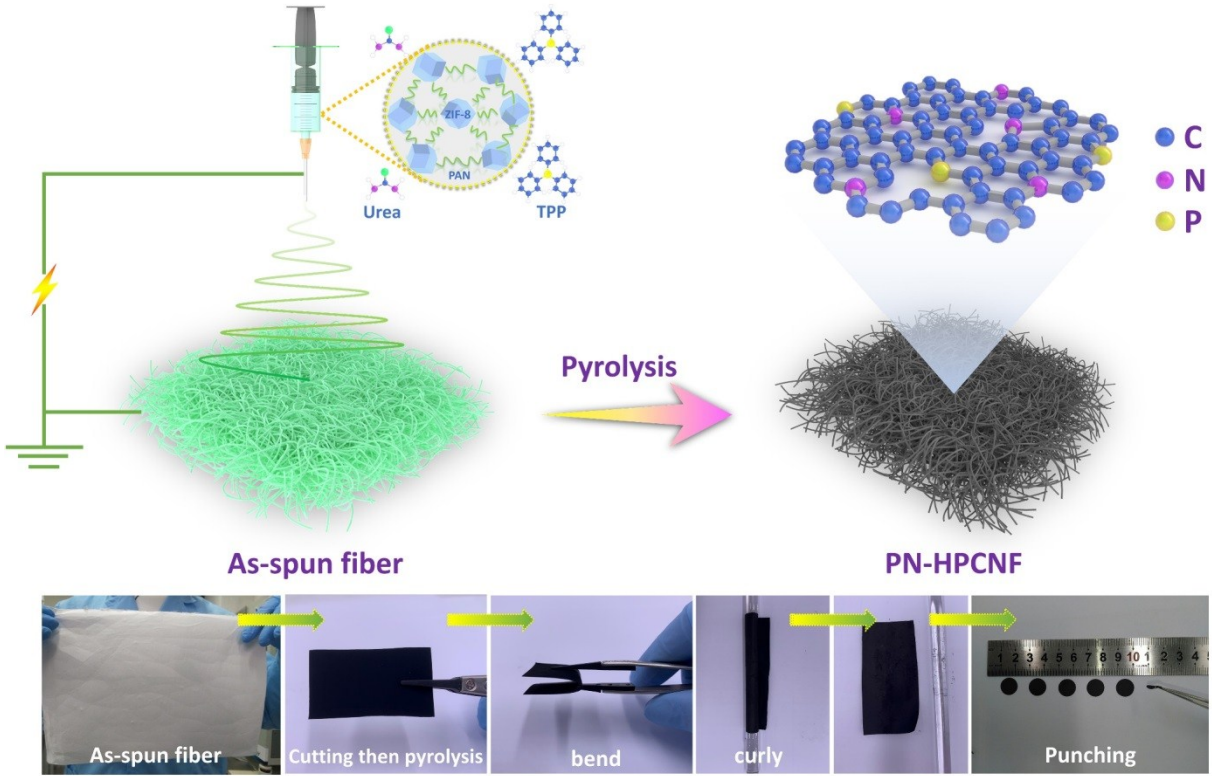

Figure S1. Schematic illustration of the preparation process for the PN-HPCNF.

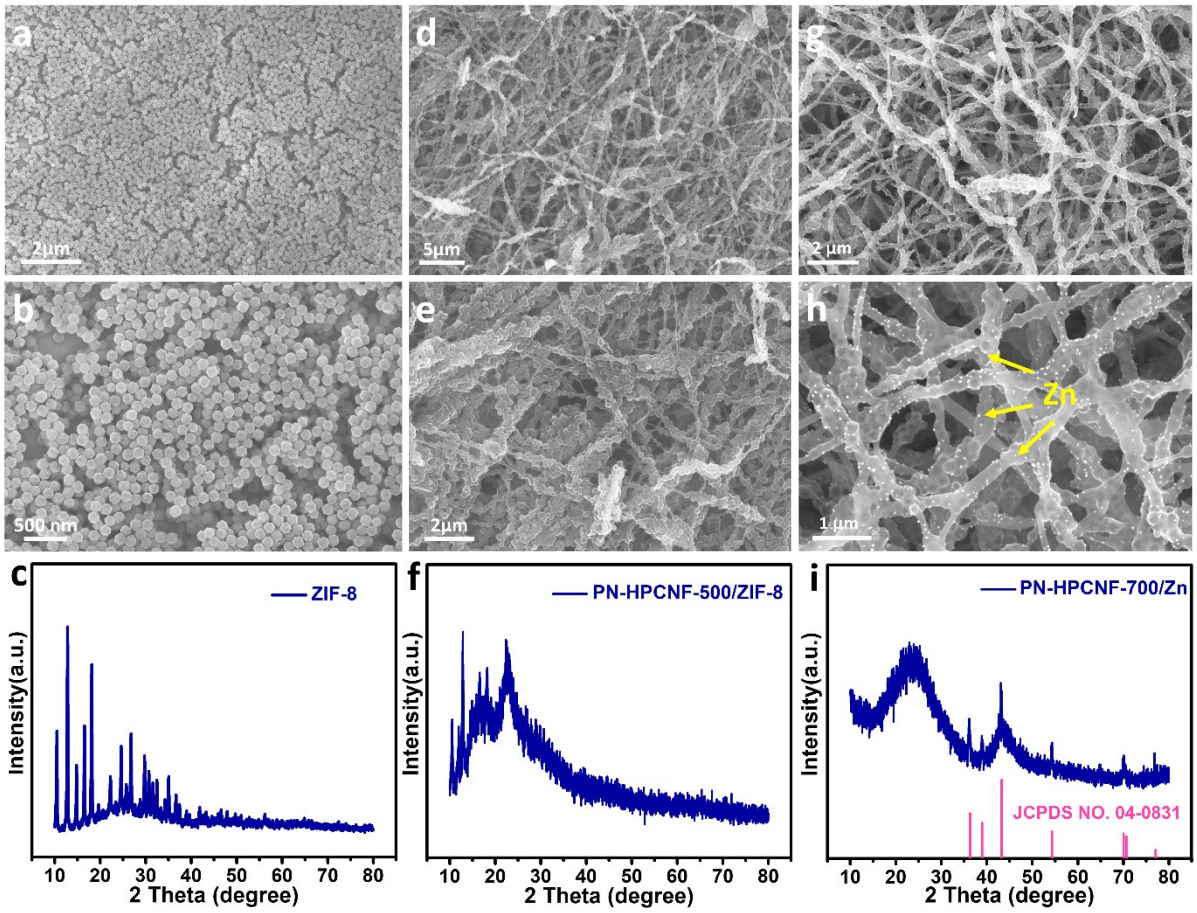

Figure S2. (a, b) FESEM images and (c) XRD pattern of ZIF-8, (d, e) FESEM images and (f) XRD pattern of PN-HPCNF at 500℃ (PN-HPCNF-500/ZIF-8), (g, h) FESEM images and (i) XRD pattern of PN-HPCNF at 700℃ (PN-HPCNF-700/Zn).

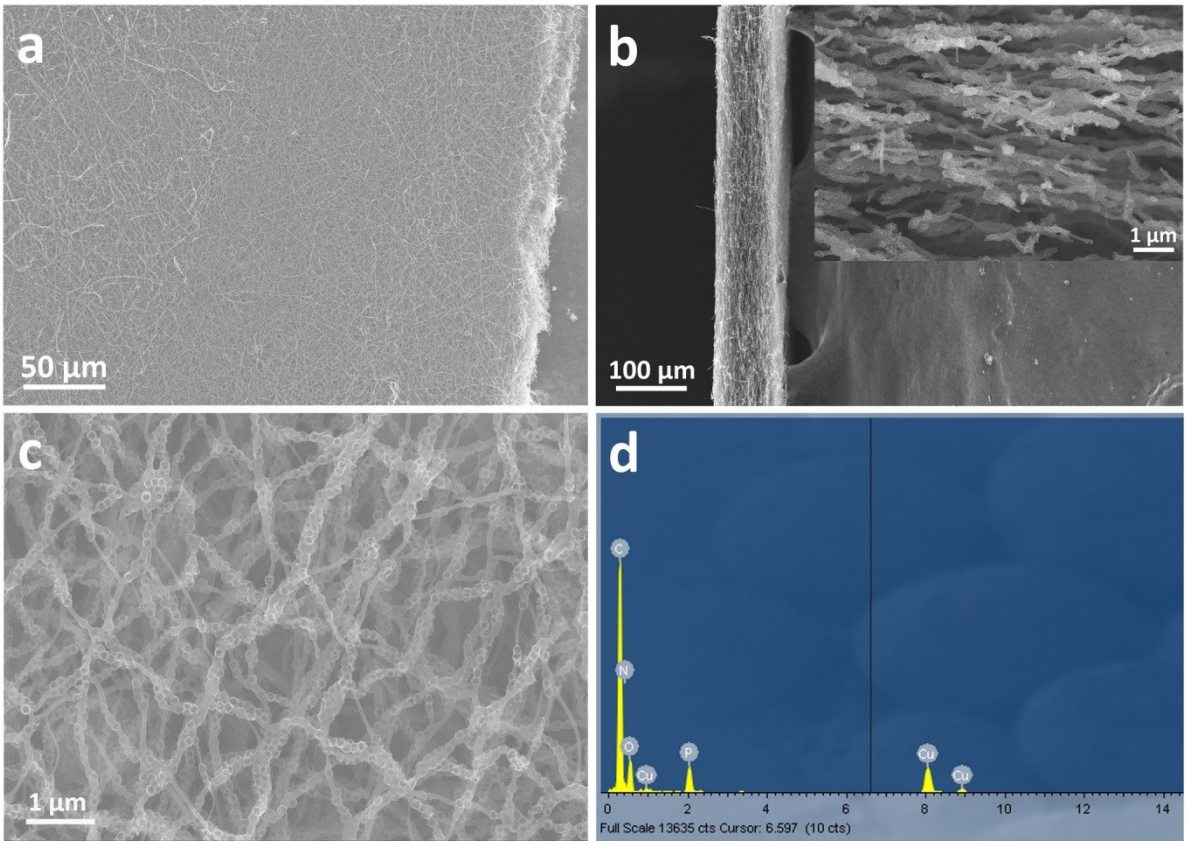

Figure S3. (a) FESEM image, (b) Cross-sectional FESEM image, (c) FESEM image and (d) EDS spectra of the PN-HPCNF.

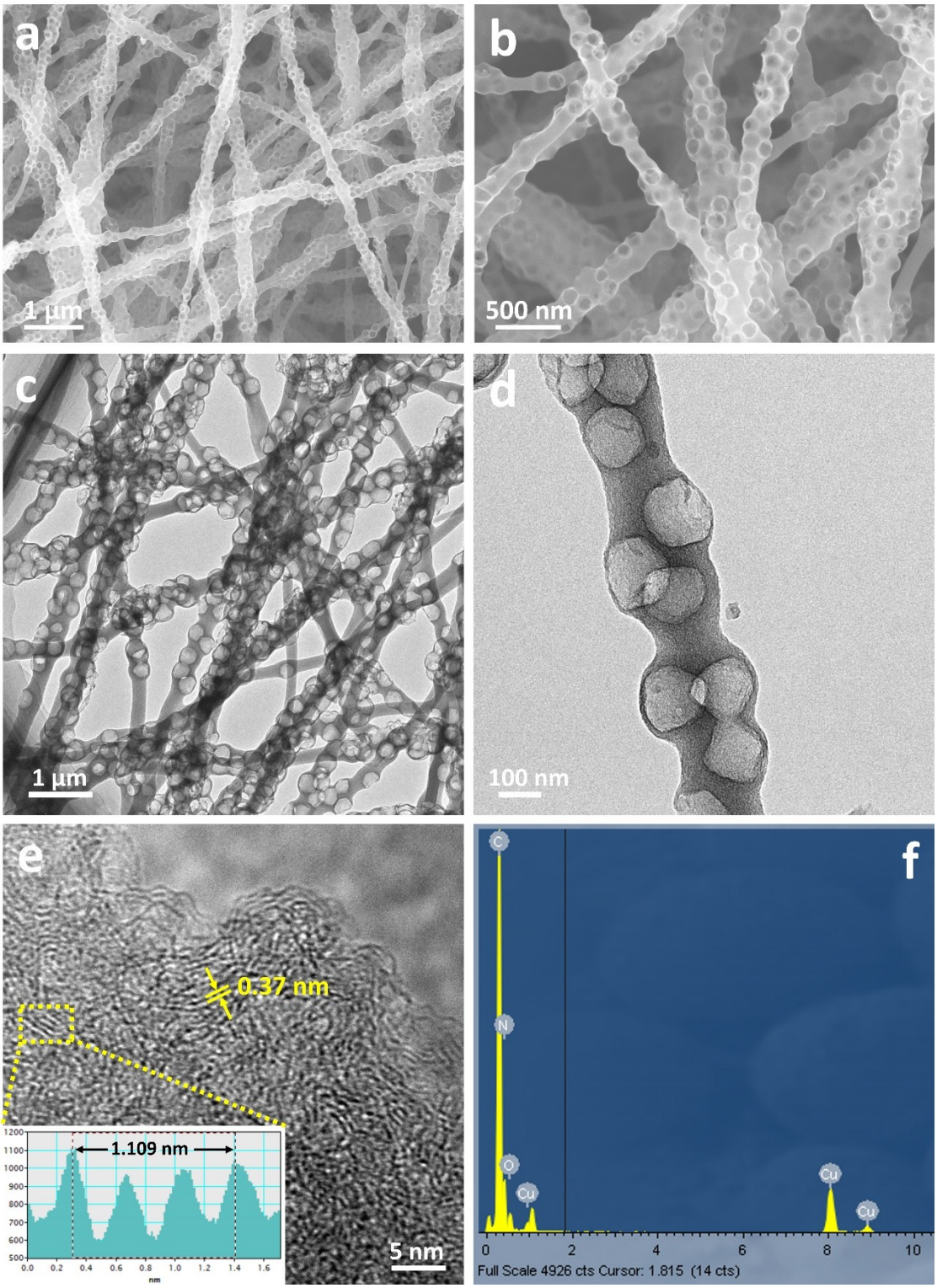

Figure S4. (a, b) FESEM images, (c, d) TEM images, (e) HRTEM image and (f) EDS spectra of the N-HPCNF.

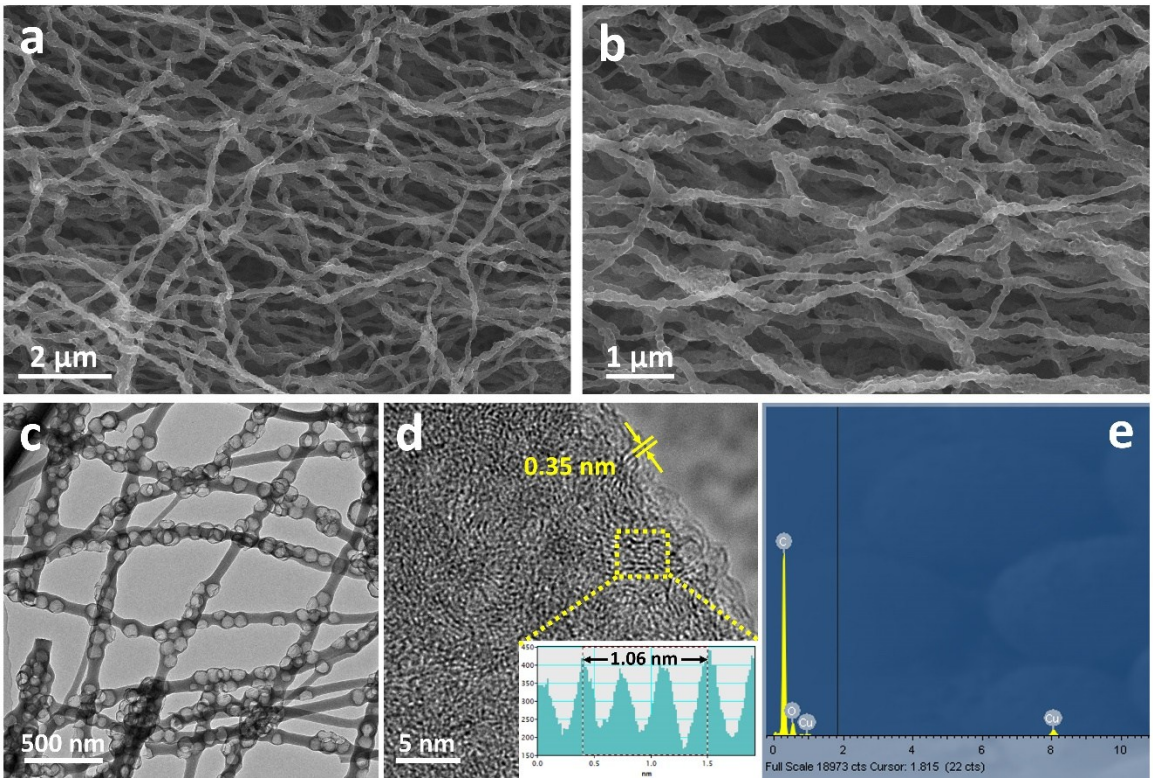

Figure S5. (a, b) FESEM images, (c) TEM image, (d) HRTEM image and (e) EDS spectra of the HPCNF.

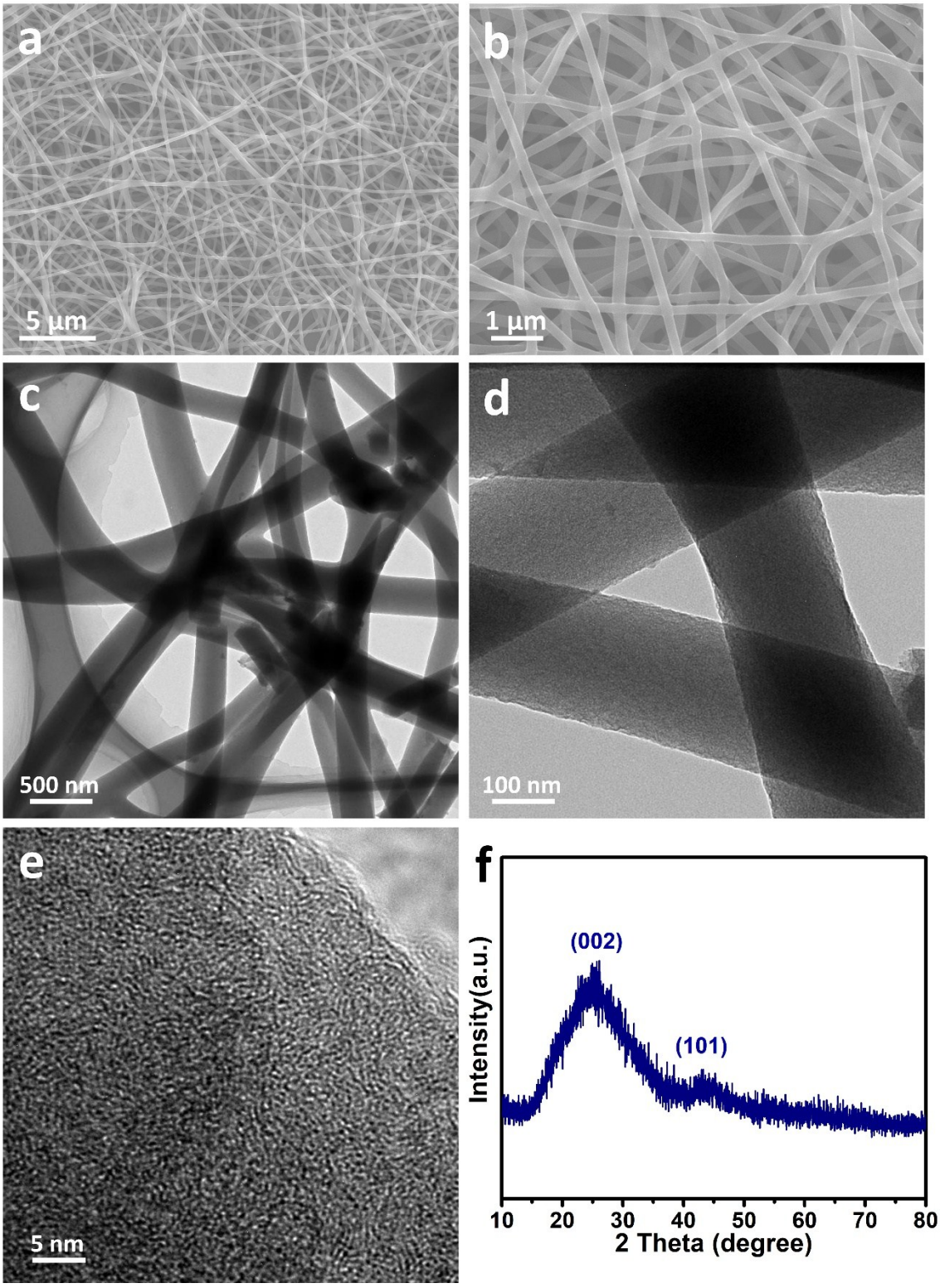

Figure S6. (a, b) FESEM images, (c, d) TEM images, (e) HRTEM image and (f) XRD pattern of the CNF.

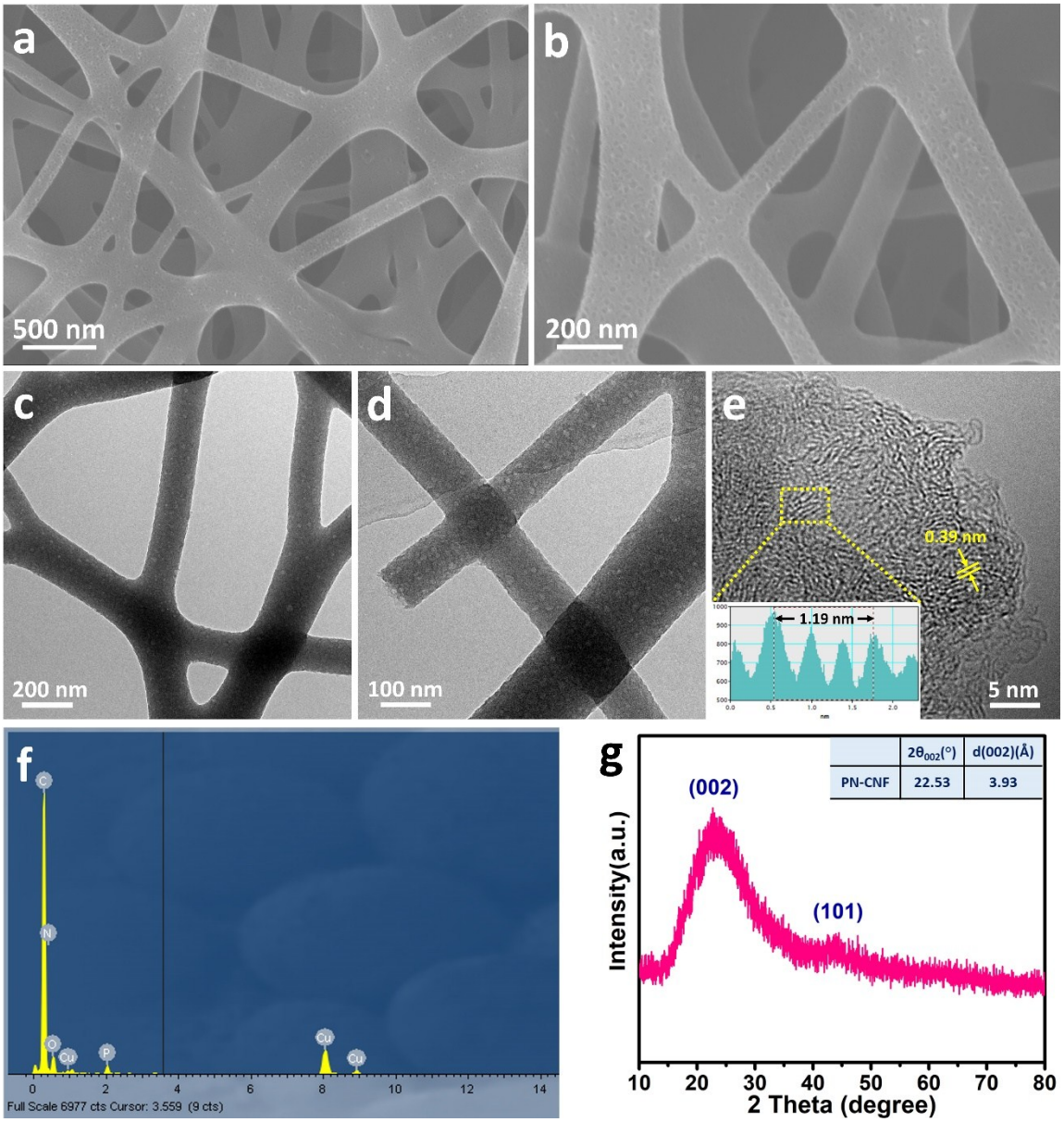

Figure S7. (a, b) FESEM images, (c, d) TEM images, (e) HRTEM image, (f) EDS spectra and (g) XRD pattern of the PN-CNF.

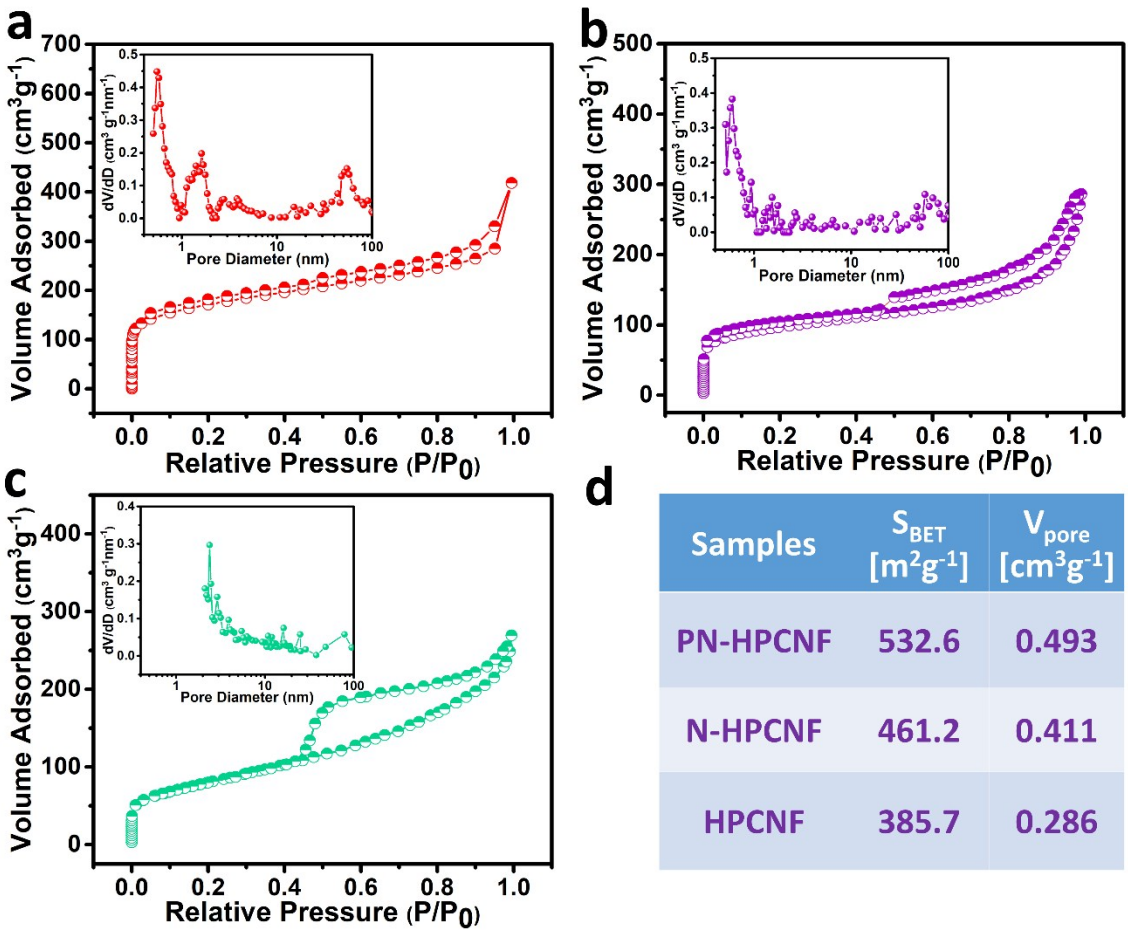

Samples	S_{BET} [m^2g^{-1}]	V_{pore} [cm^3g^{-1}]
PN-HPCNF	532.6	0.493
N-HPCNF	461.2	0.411
HPCNF	385.7	0.286

Figure S8. Nitrogen adsorption-desorption isothermal curves (inset: pore size distribution) for (a) PN-HPCNF, (b) N-HPCNF and (c) HPCNF. (d) Specific surface area and pore volume of all samples.

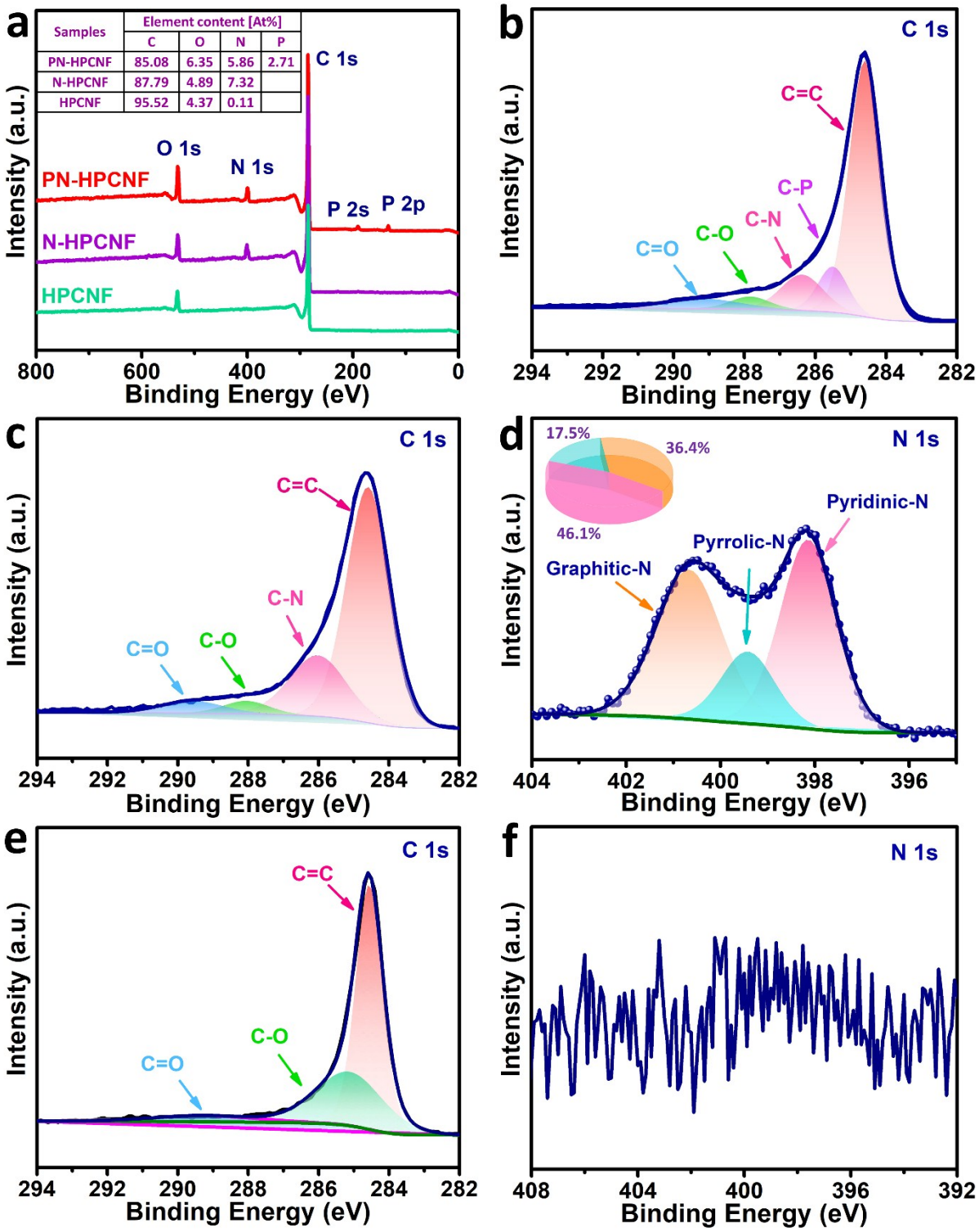

Figure S9. (a) The survey XPS spectrum of PN-HPCNF, N-HPCNF and HPCNF. The high-resolution C 1s spectra of (b) PN-HPCNF and (c) N-HPCNF. (d) The high-resolution N 1s spectra of N-HPCNF. (e, f) The high-resolution C 1s and N 1s spectra of HPCNF.

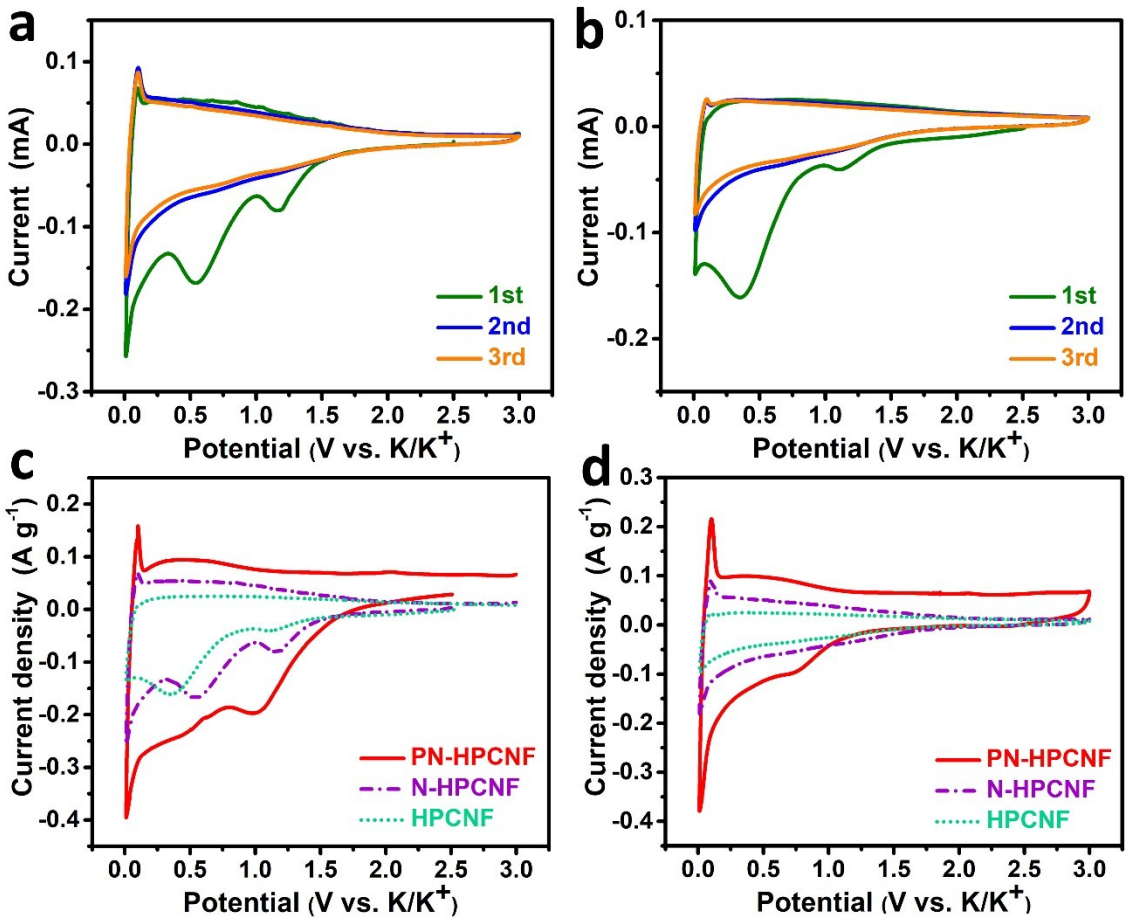

Figure S10. CV curves of the (a) N-HPCNF and (b) HPCNF electrodes at a scan rate 0.1 mV s^{-1}. CV curves of the PN-HPCNF, N-HPCNF and HPCNF electrodes at a scan rate 0.1 mV s^{-1} for the (c) 1st cycle and (d) 2nd cycle.

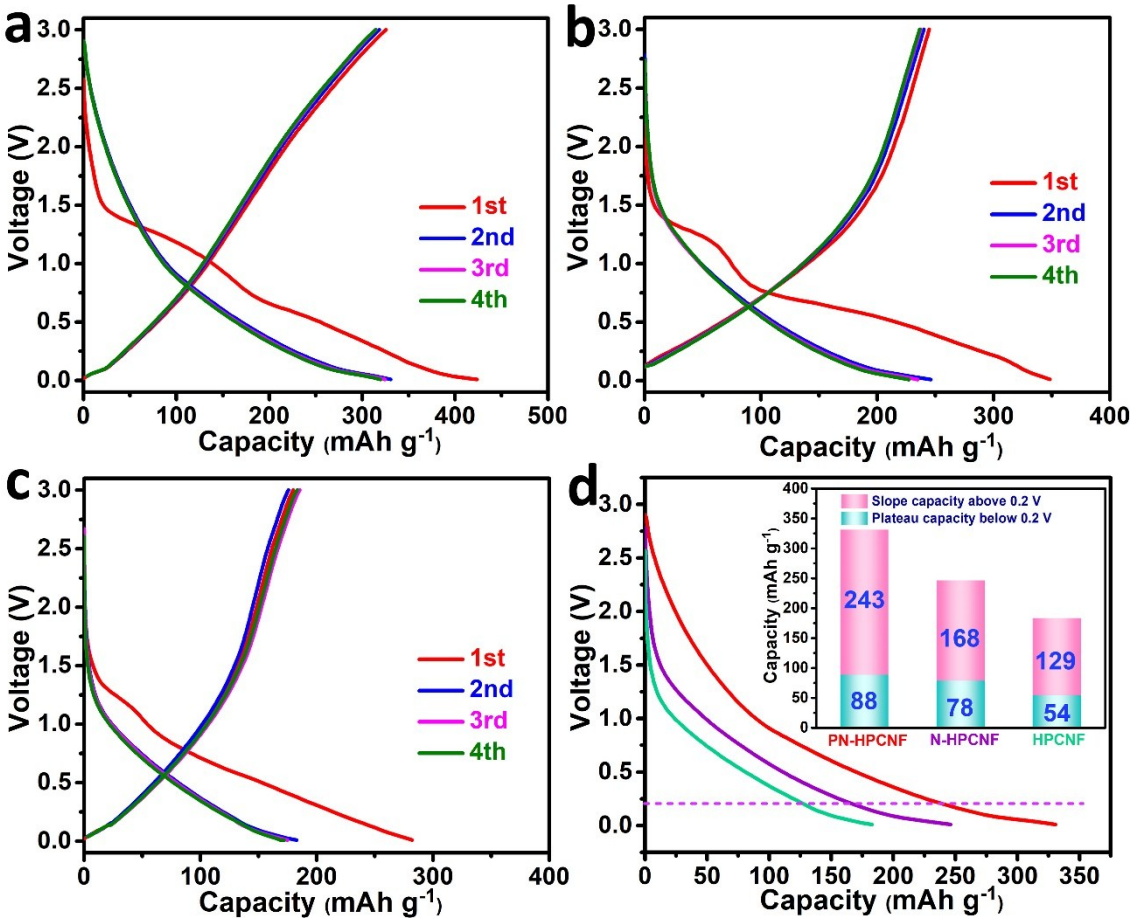

Figure S11. Charge-discharge profiles of (a) PN-HPCNF, (b) N-HPCNF and (c) HPCNF electrodes the at current density of 0.2 A g^{-1}. (d) The discharge profiles of PN-HPCNF, N-HPCNF and HPCNF at second cycle (inset: the capacity contribution at each stage).

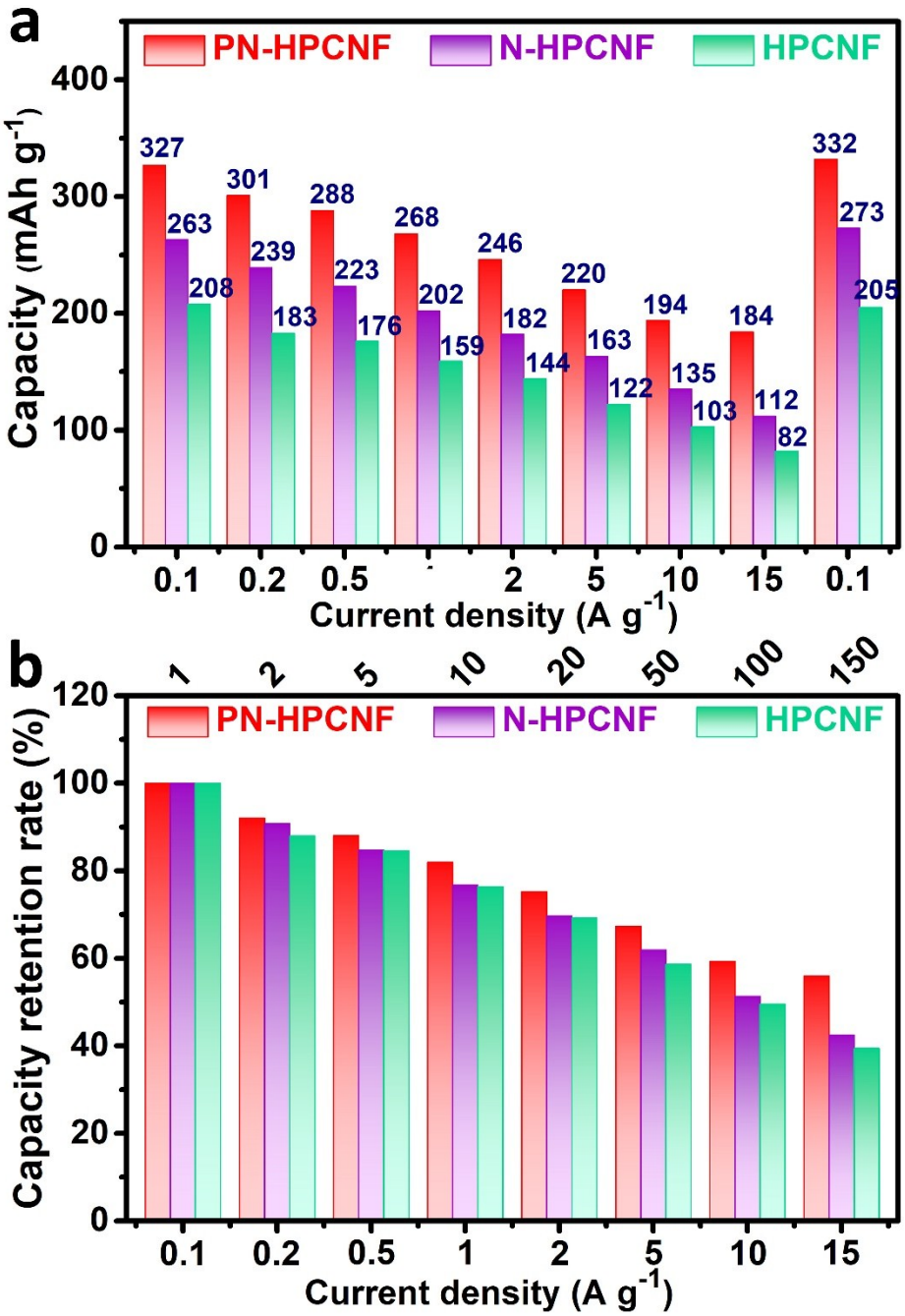

Figure S12. (a) The average capacities and (b) capacity retention rate of the three carbon electrodes at different current densities for PIBs corresponding to Figure 2c.

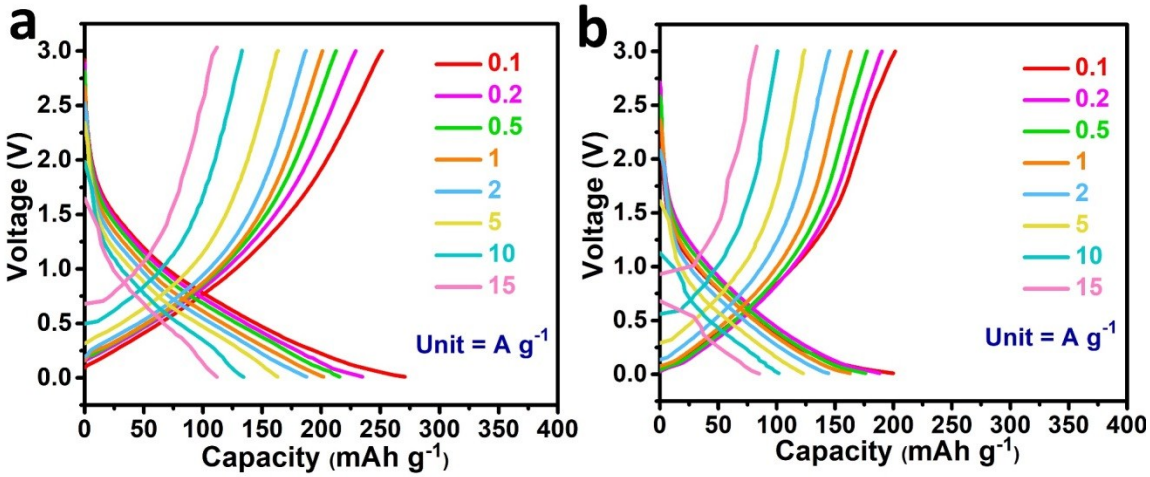

Figure S13. Charge-discharge profiles of the (a) N-HPCNF and (b) HPCNF electrodes for PIBs at current density of 0.2 A g^{-1}.

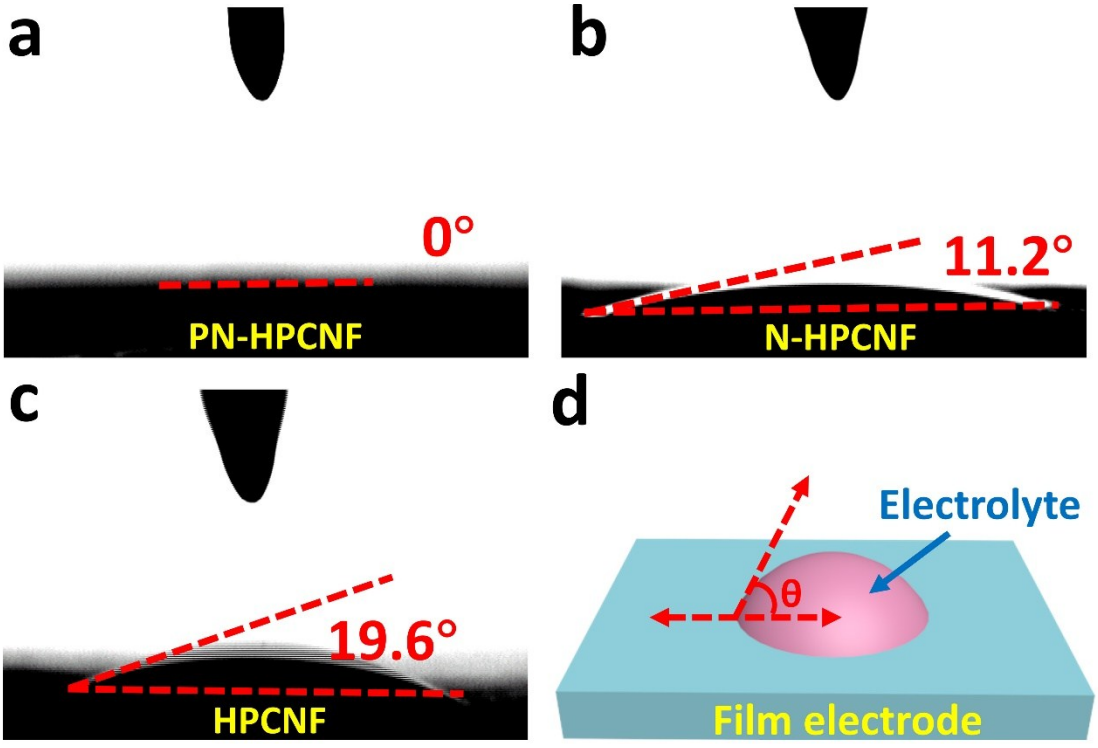

Figure S14. The electrolyte contact angle of (a) PN-HPCNF, (b) N-HPCNF and (c) HPCNF free-standing electrodes. (d) A schematic representation showing thermodynamic surface tensions.

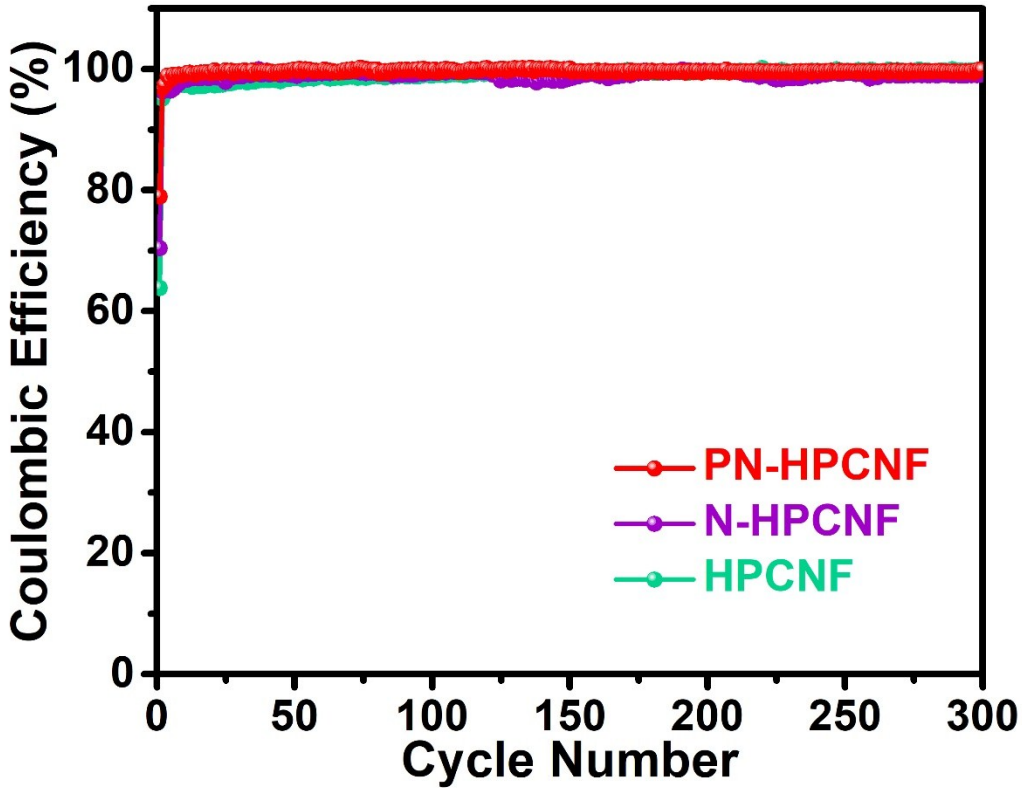

Figure S15. Coulombic dfficiency of the PN-HPCNF, N-HPCNF and HPCNF electrodes for PIBs at a current density of 0.2 A g^{-1} for 300 cycles.

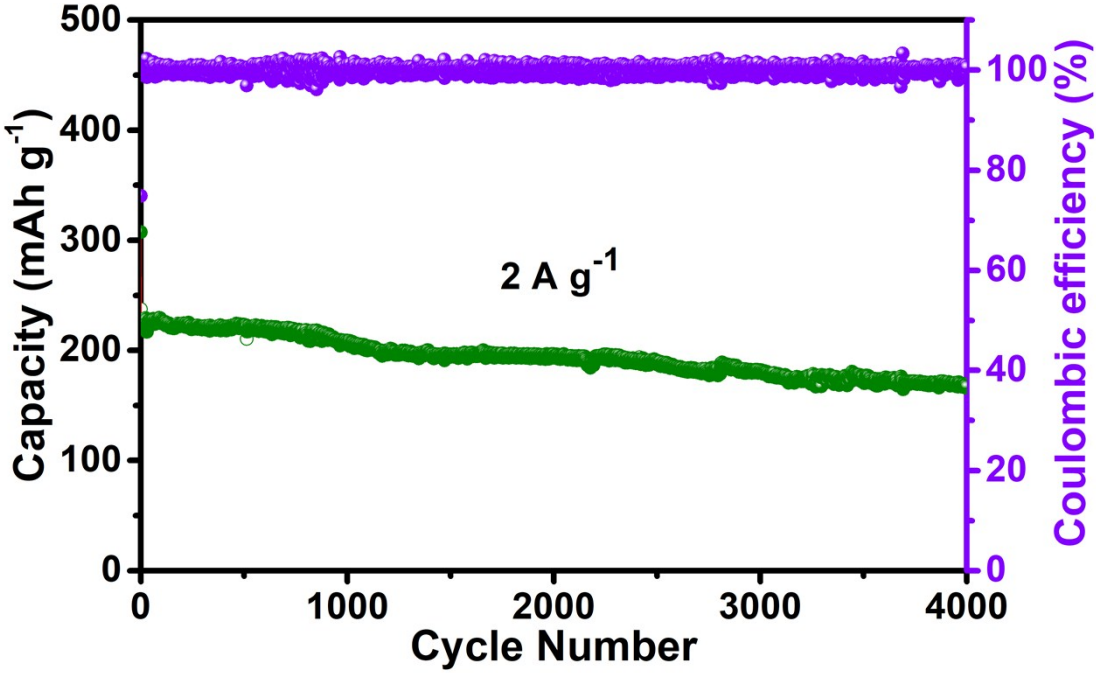

Figure S16. Long-term cycling performance of the PN-CNF at 2.0 A g^{-1}.

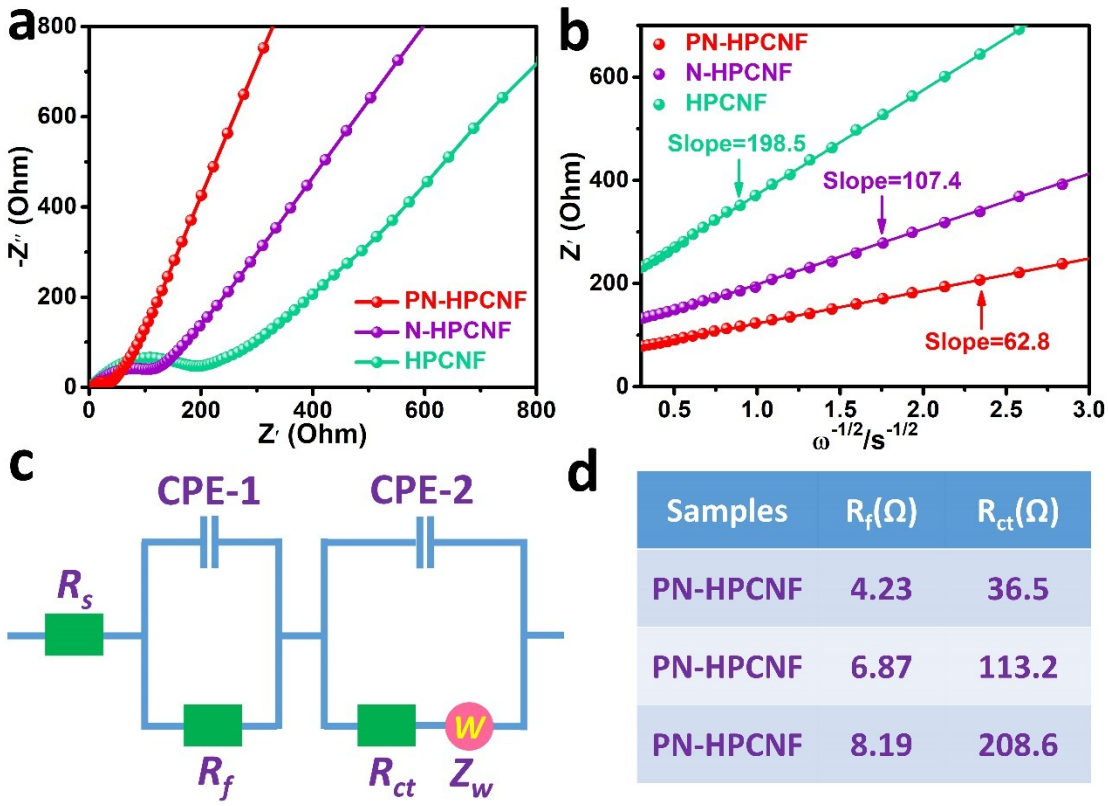

Samples	$R_f(\Omega)$	$R_{ct}(\Omega)$
PN-HPCNF	4.23	36.5
PN-HPCNF	6.87	113.2
PN-HPCNF	8.19	208.6

Figure S17. (a) Electrochemical impedance spectra (EIS) of the PN-HPCNF, N-HPCNF and HPCNF electrodes and (b) linear fits of the Z` versus $\omega^{-1/2}$ ($\omega = 2\pi f$) in the low-frequency region. (c) the corresponding equivalent circuit model. (d) The EIS fitting parameters of PN-HPCNF, N-HPCNF and HPCNF electrodes.

The equivalent circuit of EIS spectra was modeled to fit the Nyquist plots, where R_s, R_{ct} and R_f represent the total ohmic resistance of the electrode system, charge-transfer resistance in the middle-frequency region and SEI films resistance in the high-frequency region, respectively. Zw is the Warburg impedance for K^+ diffusion in the bulk of the electrode materials associated with the straight sloping line at low frequency region. CPE-1 and CPE-2 related to the surface capacitance and double layer capacitance, respectively.

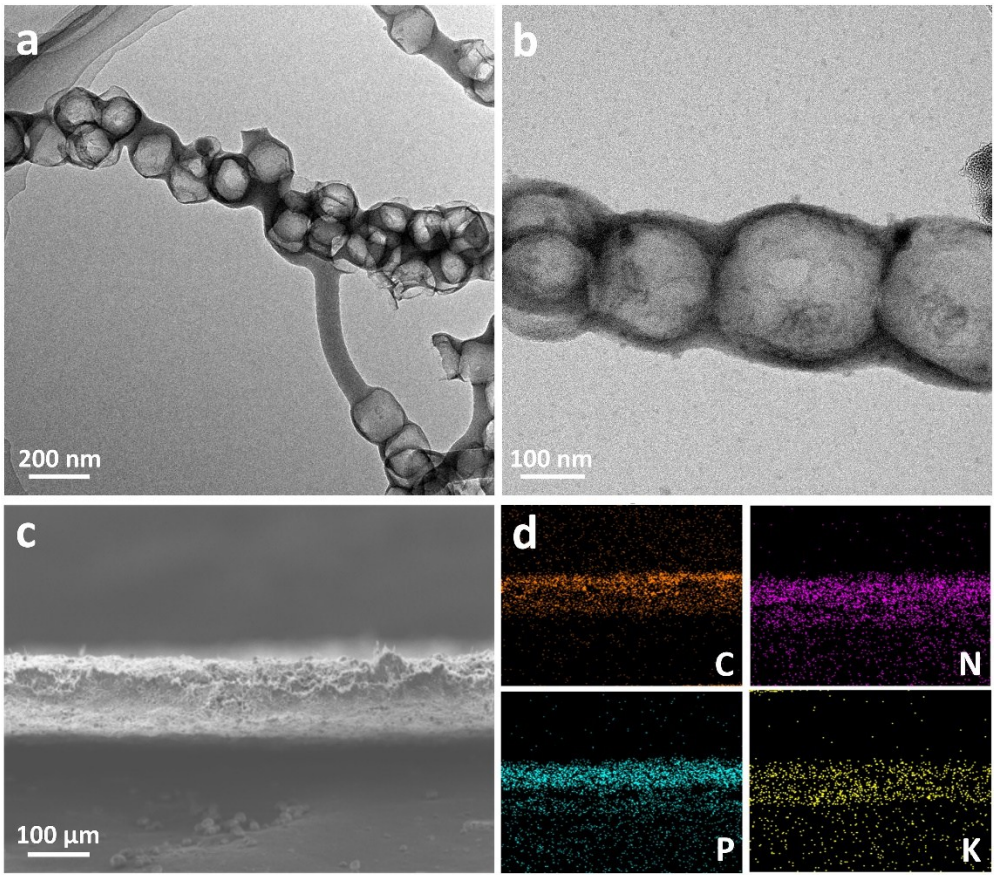

Figure S18. (a, b) TEM images, (c) Cross-sectional FESEM image and (d) corresponding elemental mapping images of PN-HPCNF electrode at full potassiation state after the 10th cycles at 0.2 A g^{-1} for PIBs.

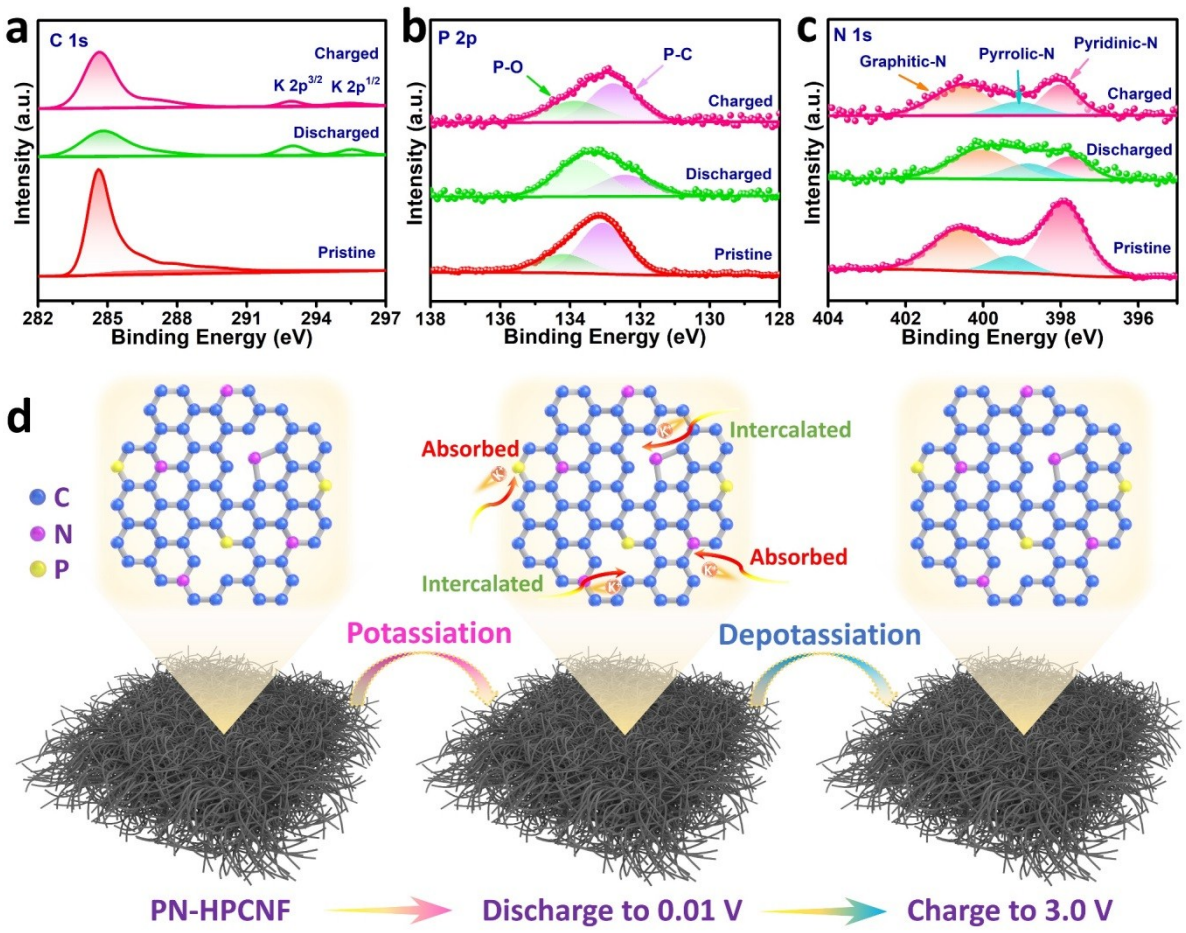

Figure S19. The ex-situ XPS analysis of (a) C 1s, (b) P 2p, and (c) N 1s spectra for the PN-HPCNF electrode at different discharge/charge stages. (d) schematic illustration of reversible electrochemical reaction mechanism of the PN-HPCNF.

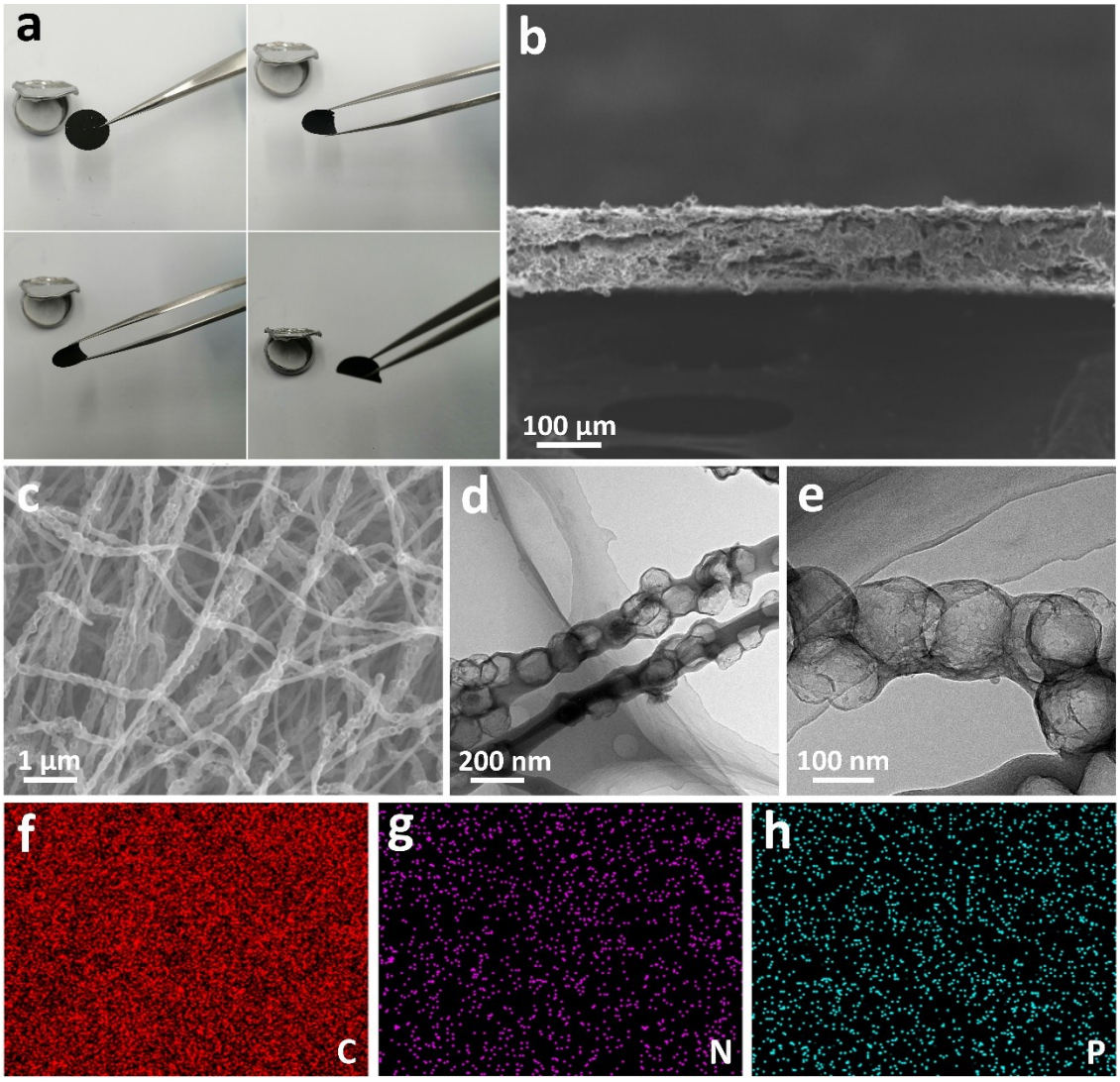

Figure S20. (a) Camera photo, (b) Cross-sectional FESEM image, (c) Top view FESEM image, (d, e) TEM images and (f-h) corresponding elemental mapping images of PN-HPCNF electrode at current density of 0.2 A g^{-1} after 300 cycles for PIBs.

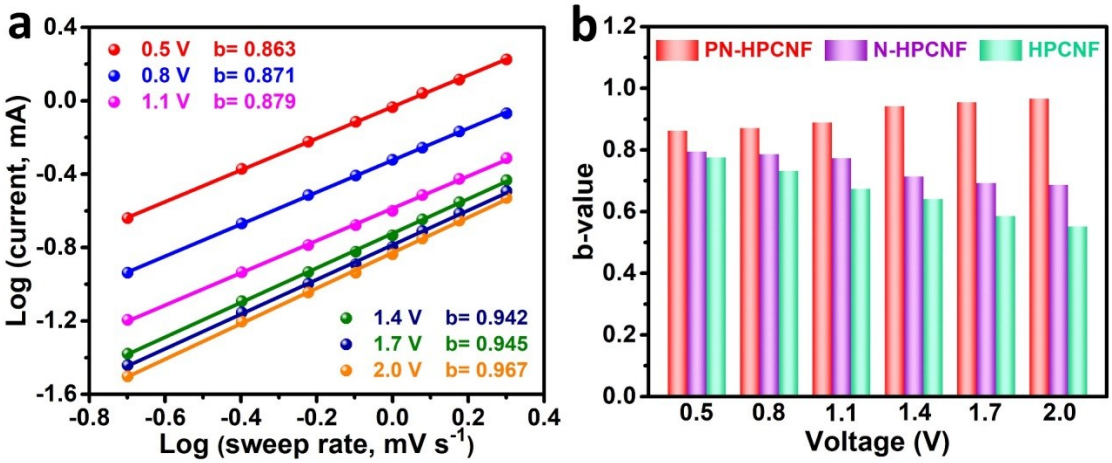

Figure S21. (a) Linear relationships between logarithm currents and logarithm sweep rate of PN-HPCNF curves. (b) b values of PN-HPCNF, N-HPCNF and HPCNF at different voltage for cathodic scans.

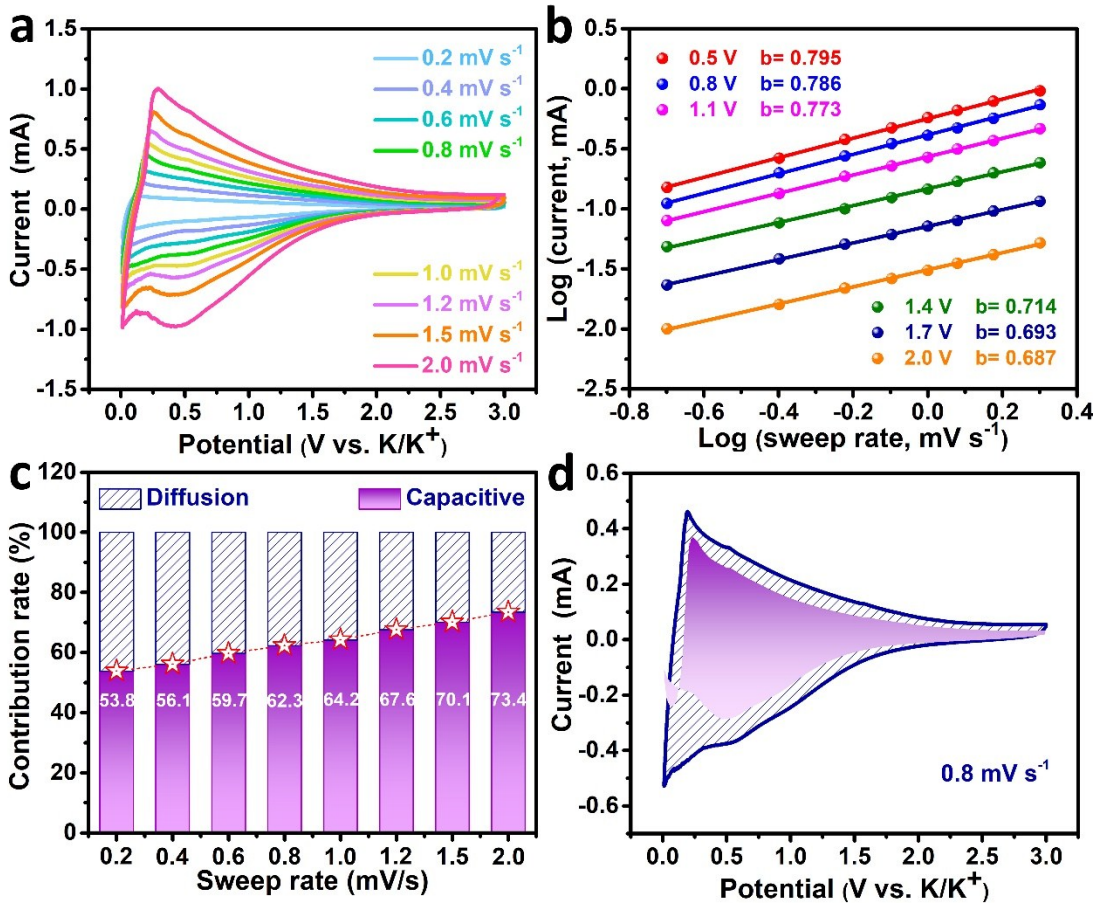

Figure S22. (a) CV curves at various scan rates from 0.2 to 2.0 mV s^{-1}, (b) Linear relationships between logarithm currents and logarithm sweep rate, (c) normalized contribution ratio of capacitive and diffusion at different scan rates and (d) capacitive contribution at 0.8 mV s^{-1} of N-HPCNF electrode.

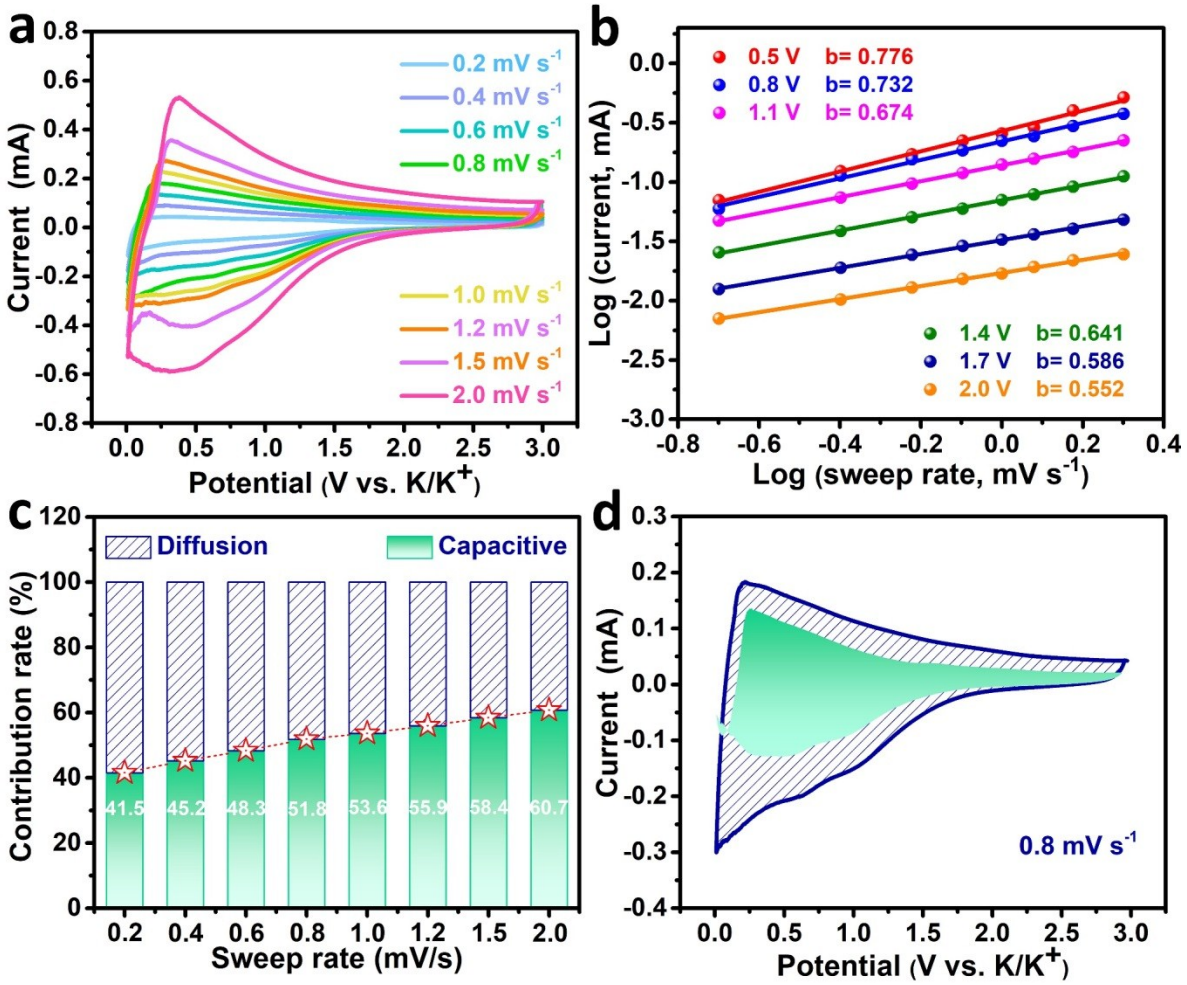

Figure S23. (a) CV curves at various scan rates from 0.2 to 2.0 mV s^{-1}, (b) Linear relationships between logarithm currents and logarithm sweep rate, (c) normalized contribution ratio of capacitive and diffusion at different scan rates and (d) capacitive contribution at 0.8 mV s^{-1} of HPCNF electrode.

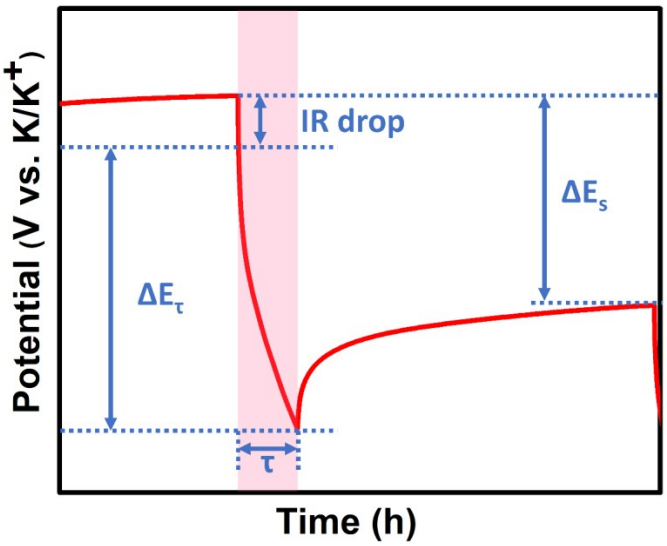

Figure S24. The value of D_K can be calculated according to the simplified Fick's second law with the following equation:

$$D = \frac{4}{\pi\tau}\left(\frac{m_B V_M}{M_B A}\right)^2\left(\frac{\Delta E_s}{\Delta E_\tau}\right)^2 \quad \text{(Equation S5)}$$

where τ is the duration of the current pulse, m_B is the electrode active mass, M_B and V_M denotes the molar mass and molar volume of electrode material, A is the geometric area of electrode, ΔEs is the quasi-thermodynamic equilibrium potential difference between before and after the current pulse regardless of the IR-drop. ΔEτ represents the change of voltage during the current pulse. The relative value of M_B/V_M can be obtained from the density of materials, which is calculated according to the following equation:

$$\rho = \frac{1}{V_{total} + \frac{1}{\rho_{carbon}}} \quad \text{(Equation S6)}$$

where ρ (g cm^{-3}) is the density of materials, V_{total} (cm^3 g^{-1}) is the total pore volume determined from the N_2 isotherm, and ρ_{carbon} is the true density of carbon (2 g cm^{-3}).

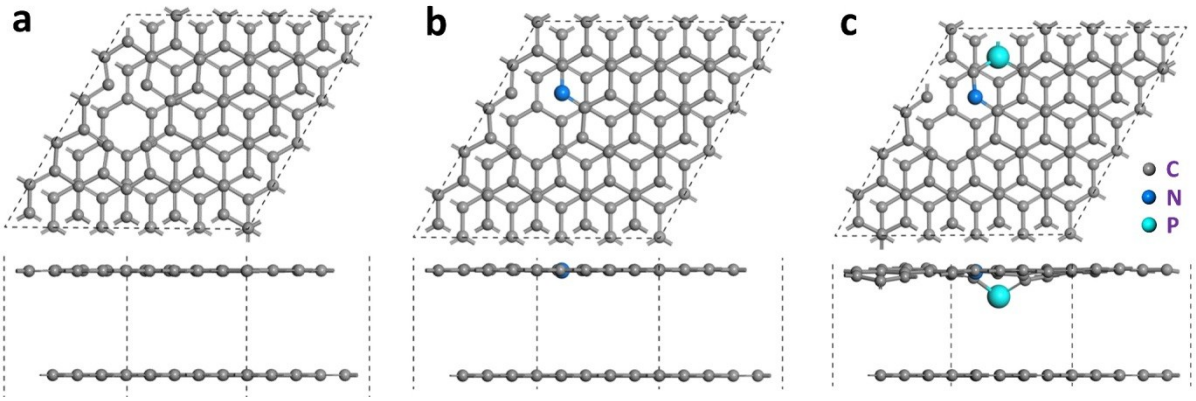

Figure S25. Top and side view of the optimized structure of (a) HPCNF, (b) N-HPCNF and (c) PN-HPCNF.

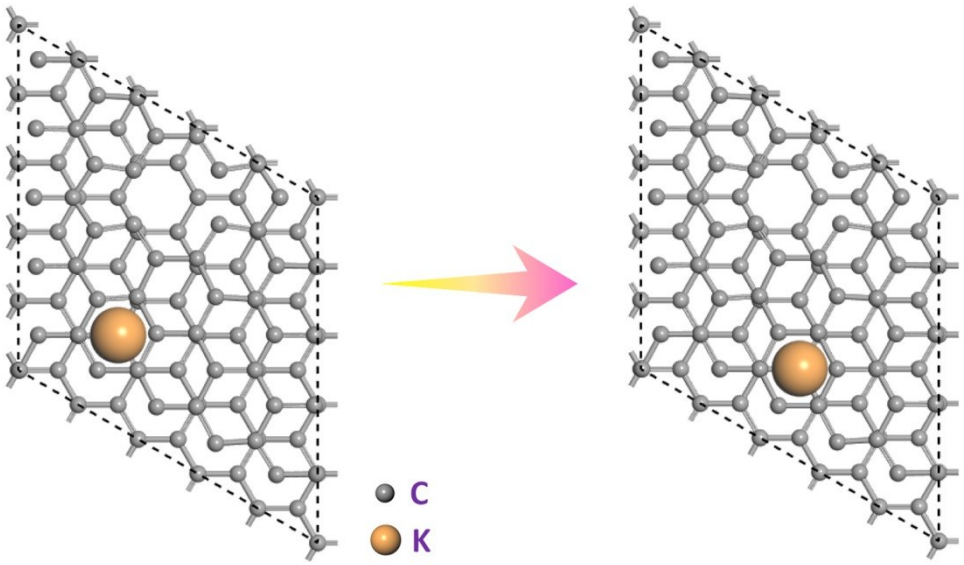

Figure S26. Illustration of the K ion diffusion path from one hollow position to the nearest hollow position in HPCNF.

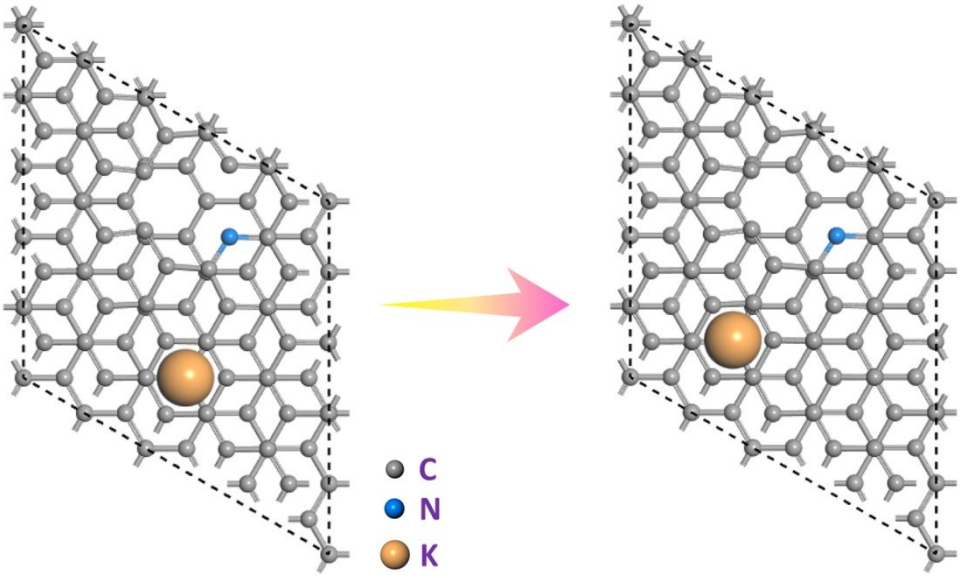

Figure S27. Illustration of the K ion diffusion path from one hollow position to the nearest hollow position in N-HPCNF.

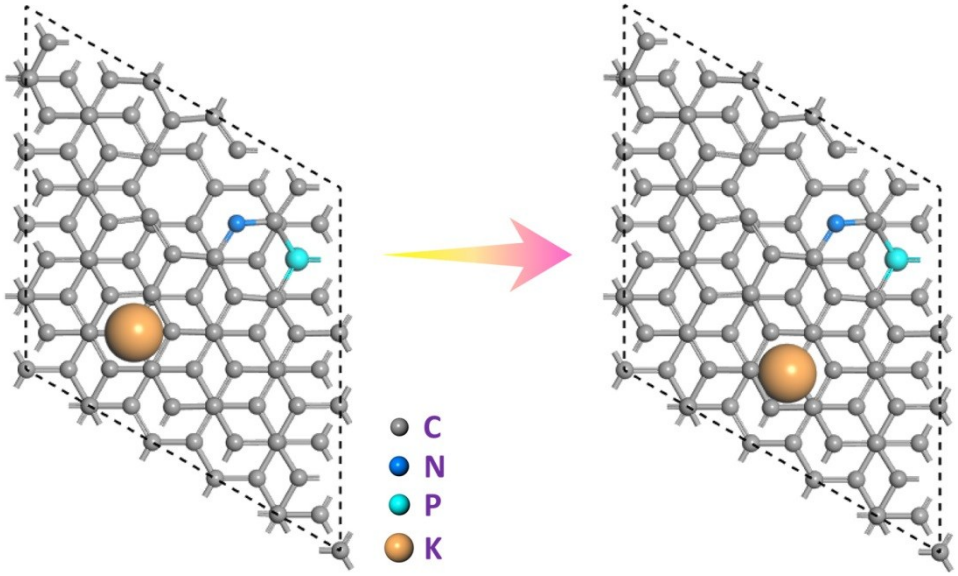

Figure S28. Illustration of the K ion diffusion path from one hollow position to the nearest hollow position in PN-HPCNF.

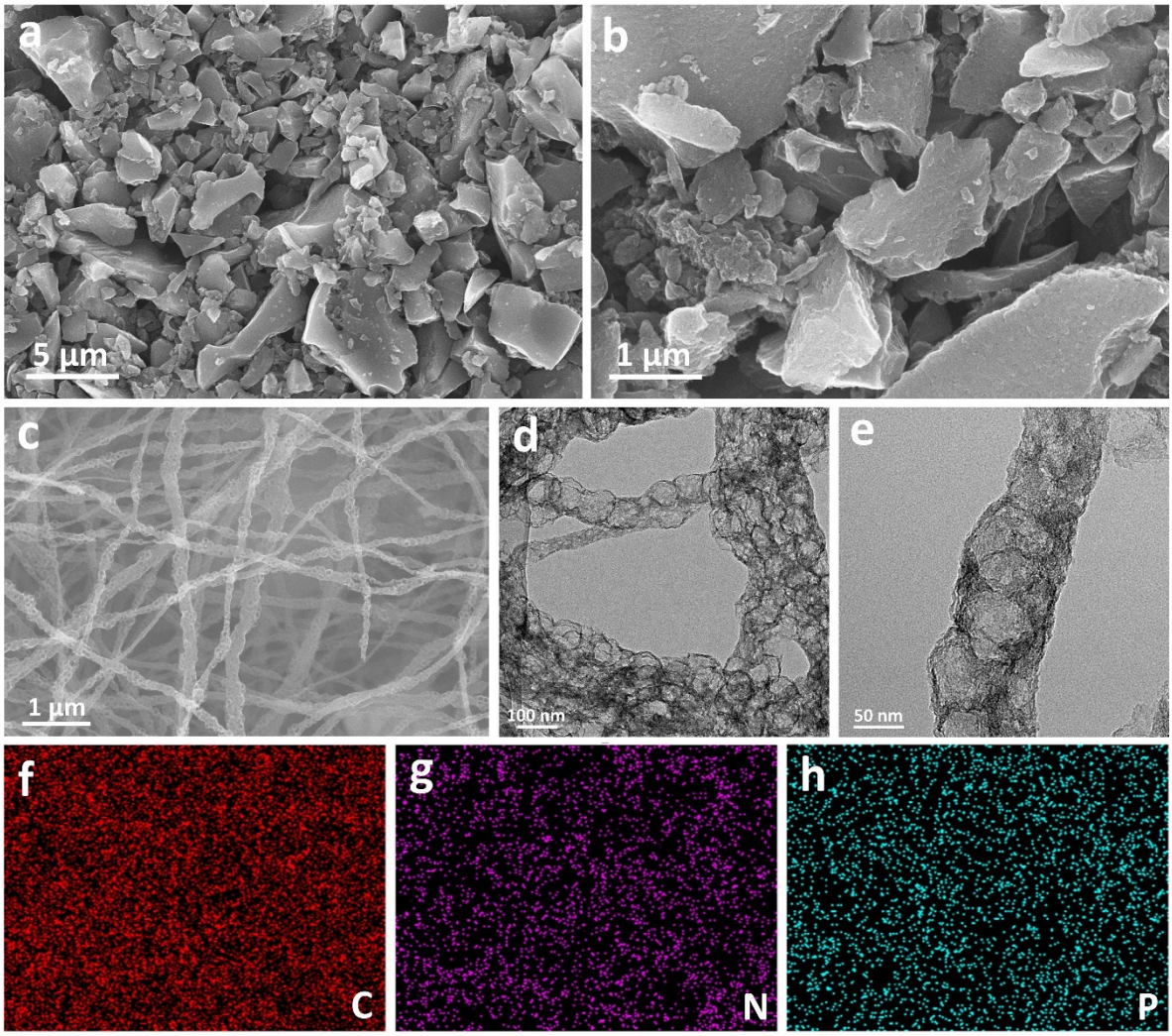

Figure S29. (a, b) FESEM images of the commercial AC. (c) FESEM image, (d, e) TEM images, and (f-h) corresponding elemental mapping images of APN-HPCNF.

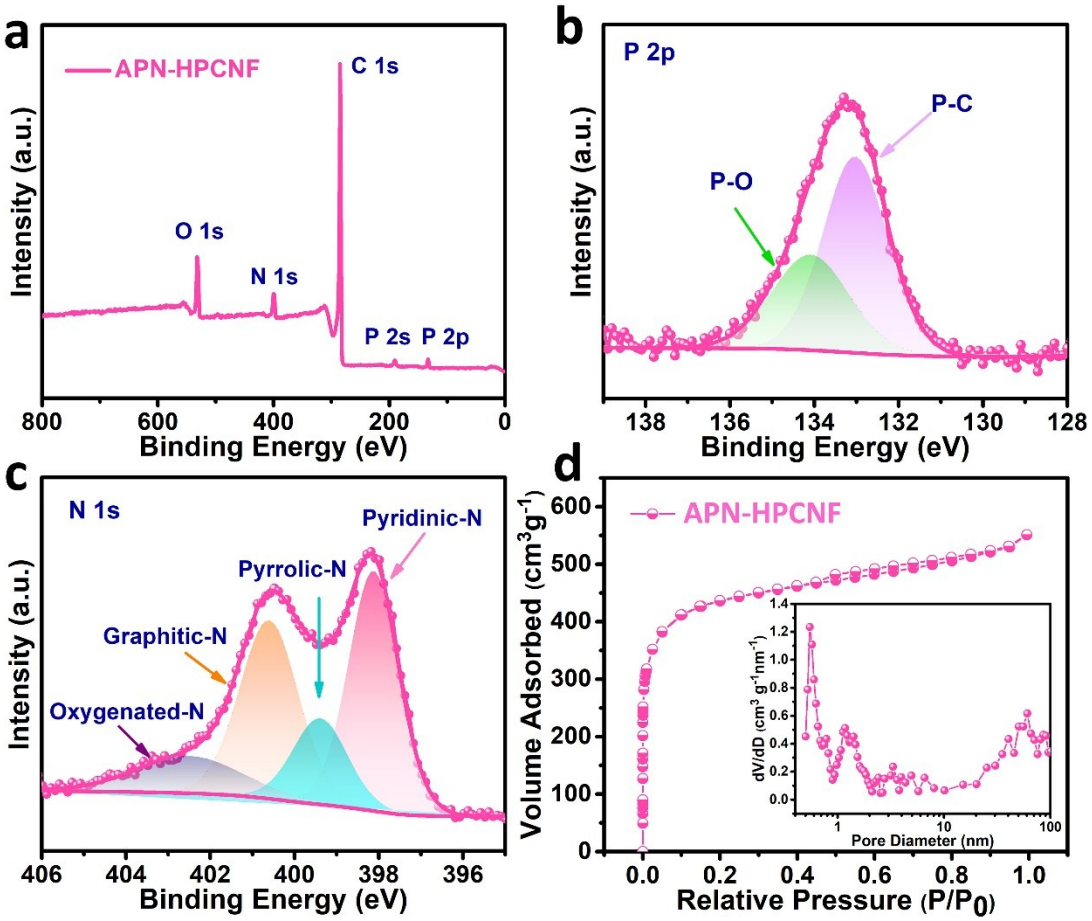

Figure S30. (a) The survey XPS spectrum, (b) high-resolution P 2p spectra, (c) high-resolution N 1s spectra, (d) nitrogen adsorption-desorption isothermal curves (inset: pore size distribution) of the APN-HPCNF.

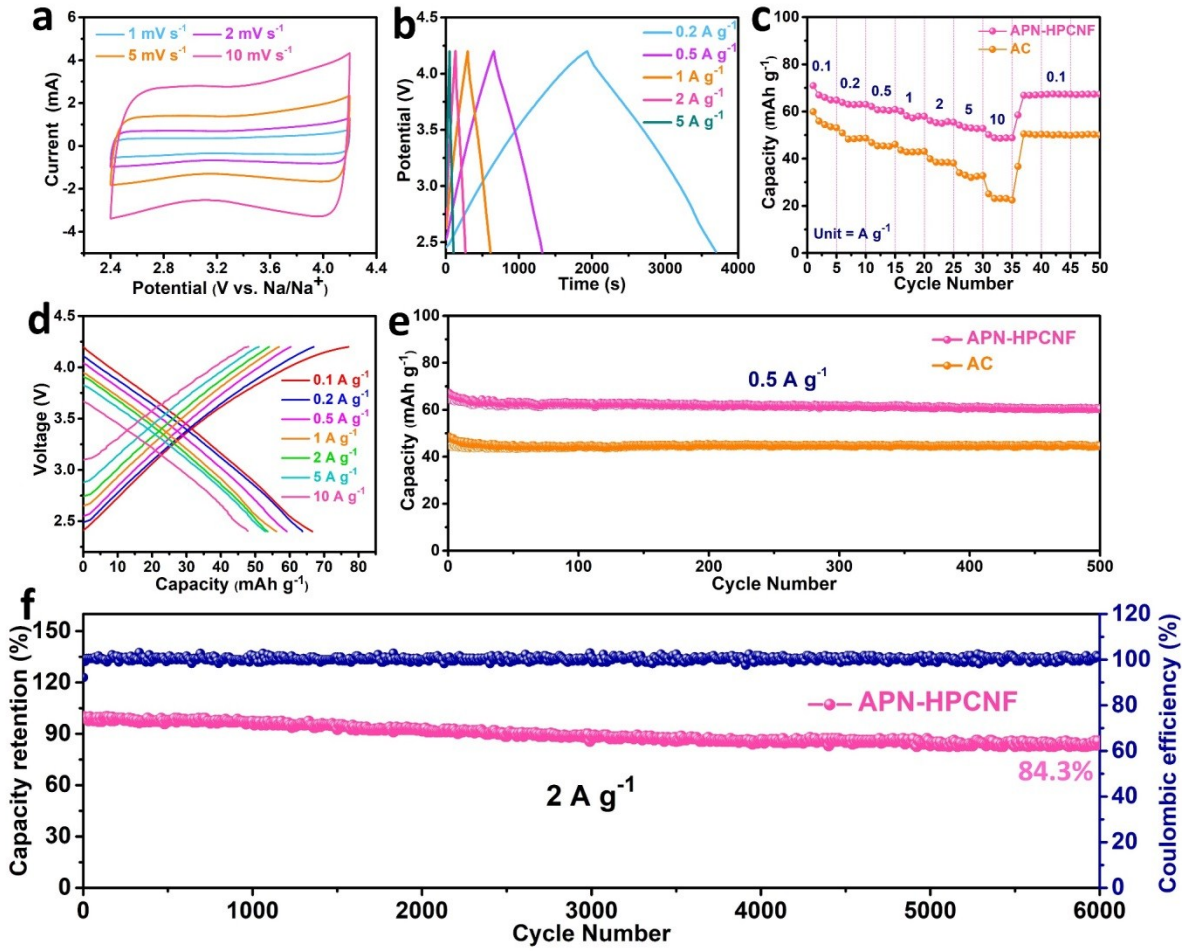

Figure S31. (a) CV curves at different scan rates and (b) GCD curves at various current densities of APN-HPCNF, (c) Rate property of APN-HPCNF and AC. (d) Charge/discharge curves at different current density of APN-HPCNF. (g) Cycling performance of APN-HPCNF and AC at 0.5 A g^{-1} and (f) Long-term cycle performance of the APN-HPCNF at 2 A g^{-1}.for 6000 cycles within a voltage window of 2.4-4.2 V versus K metal.

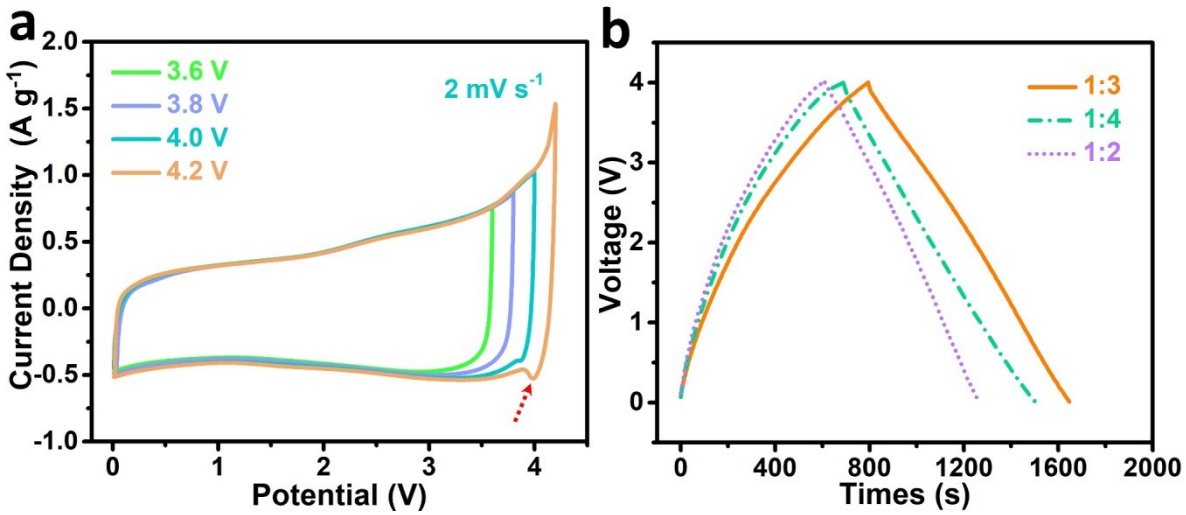

Figure S32. (a) CV curves of the APN-HPCNF//PN-HPCNF PIHCs device in different potential windows at a scan rate of 2 mV s^{-1}, (b) GCD curves of PIHCs at 0.5 A g^{-1} with different anode/cathode mass radio.

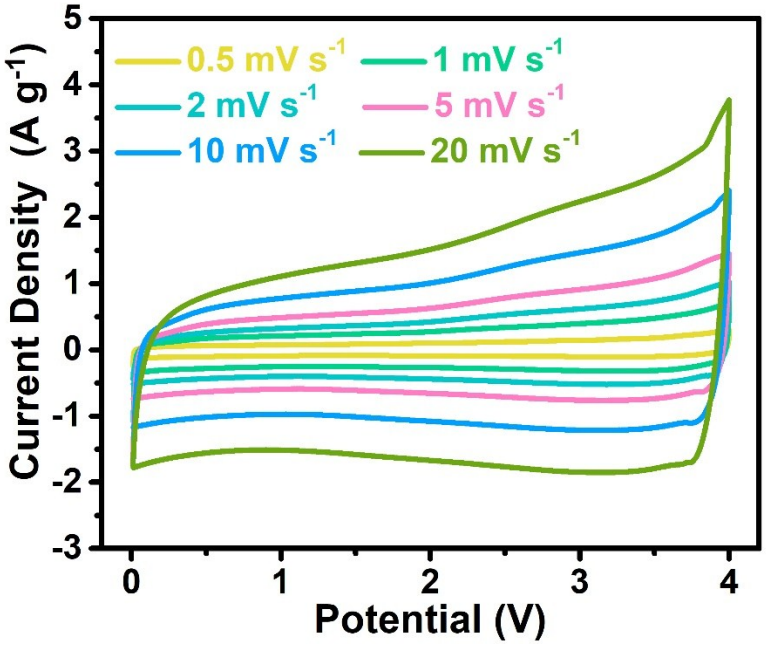

Figure S33. CV curves at different scan rates of the APN-HPCNF//PN-HPCNF PIHCs device from 0.01 to 4.0 V.

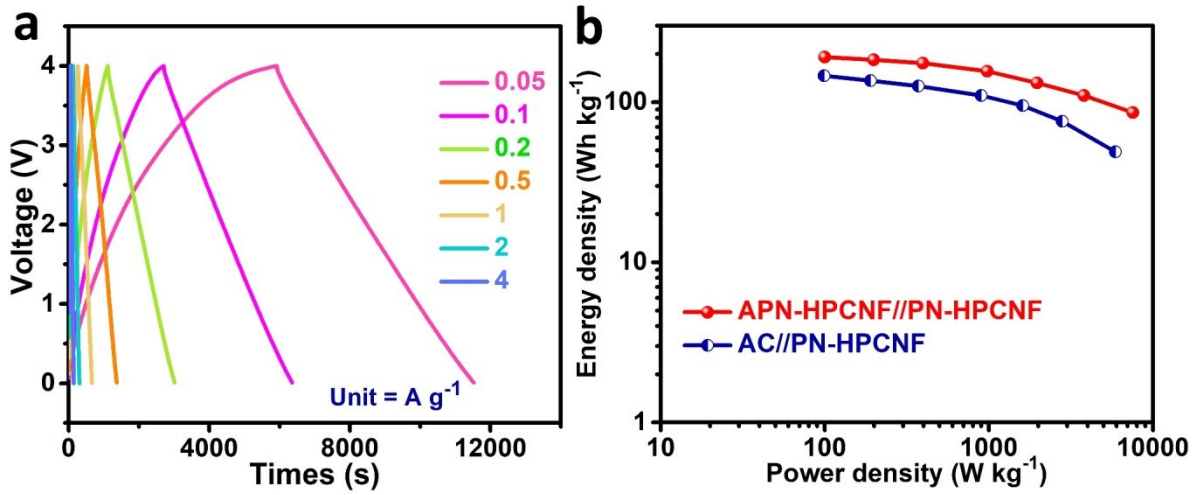

Figure S34. (a) Charge-discharge curves at different current density of the AC//PN-HPCNF PIHCs device. (b) Ragone plots of the AC//PN-HPCNF compared with APN-HPCNF//PN-HPCNF PIHCs.

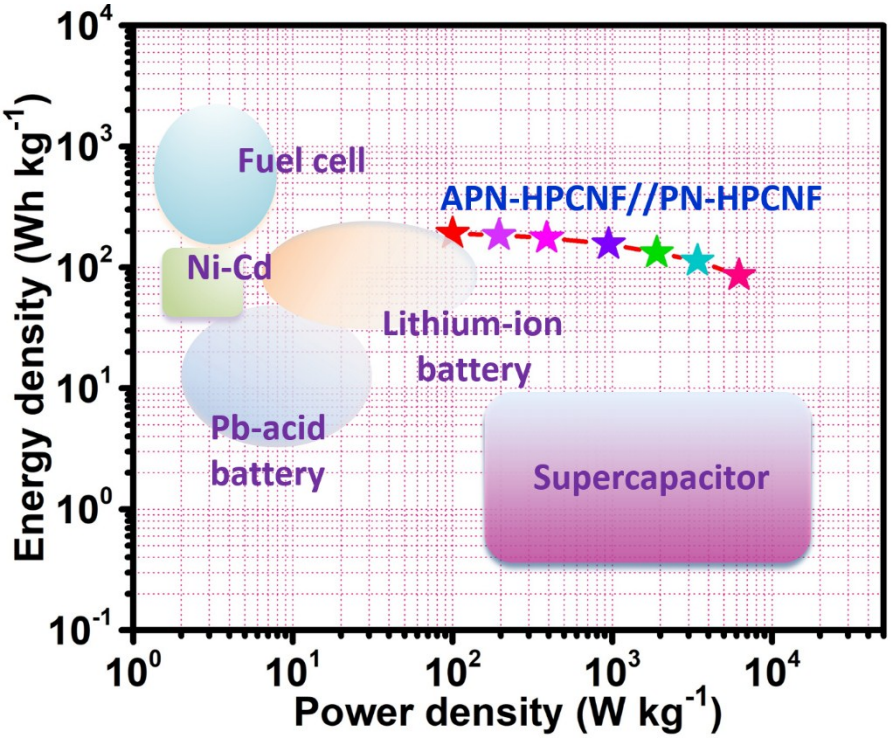

Figure S35. Ragone plots of the APN-HPCNF//PN-HPCNF PIHCs device as compared with commercial energy storage devices.

Table S1. Comparison of the initial coulombic efficiency of the carbonaceous electrodes for PIBs with our work.

Materials	Current density ($A\ g^{-1}$)	Initial coulombic efficiency	Reference
PN-HPCNF	0.2	78.9%	This work
NHC_2-NH_3/Ar	0.1	15.8%	*Energy Environ. Sci.* **2019**, 12, 1605.
PDDA-NPCNs/Ti_3C_2	0.1	73.2%	*Energy Environ. Sci.* **2020**, DOI: 10.1039/c9ee03250a.
mesoporous graphitic carbon nanospring	0.05	61.2%	*Angew. Chem. Int. Ed.* **2019**, *58,* 18108-18115
S/N@C	0.05	24.6%	*Adv. Mater.* **2019**, 31, e1805430.
Sulfur-grafted hollow carbon spheres	0.025	51.4%	*Adv. Mater.* **2019**, 31, e1900429.
P-doped hard carbon	0.1	45.7%	*Adv. Energy Mater.* **2019**, 9, 1901676.
carbon nanosheets750	0.05	38%	*Adv. Energy Mater.* **2019**, 9, 1803894.
oxygen/fluorine dual-doped porous carbon	0.1	63%	*Adv. Funct. Mater*. **2019**, 29, 1906126.
rGO aerogel	0.1	44%	*Energy Storage Mater.* **2019**, 19, 306-313.

N/O dual-doped carbon network	0.05	47.12%	*Energy Storage Mater.* **2019**, 23, 46-54
three-dimensional nitrogen-doped framework carbon	0.1	24.3%	*Energy Storage Mater.* **2019**, 23, 522-529.
P-doped N-rich honeycomb-like carbon	0.2	56.9%	*Nano Energy* **2019**, 57, 728-736.
nitrogen/oxygen codoped carbon hollow multihole bowls	0.1	63.3%	*ACS nano* **2019**, 13, 11363-11371.
N-doped carbon nanofibers-650	0.025	49%	*Nat. Commun.* **2018**, 9, 1720.
nitrogen/oxygen in situ dual-doped hierarchical porous hard carbon	0.05	25%	*Adv. Mater.* **2018**, 30, 1700104.
hierarchical carbon nanotube-S4	0.1	15%	*Adv. Mater.* **2018**, 30, e1802074.
graphitic carbon nanocage	0.05	40%	*Adv. Energy Mater.* **2018**, 8, 1801149.
nitrogen-doped porous carbon	0.1	43.1%	*Adv. Energy Mater*. **2018**, 8, 1802386.
S/O codoped porous carbon microspheres	0.05	61.7%	*Adv. Energy Mater*. **2018**, 8, 1800171.
pyridinic N-content-doped porous carbon monolith	0.02	10%	*Adv. Mater.* **2017**, 29, 1702268.

Table S2. The cycling performance comparison of PN-HPCNF and previously reported state-of-art carbonaceous materials for PIBs.

Materials	Voltage range(V)	Current density (mA g^{-1})	Cycle number	Specific capacity (mAh g^{-1})	Reference
PN-HPCNF	0.01-3.0	200	300	305	This work
		2000	10000	226	
PDDA-NPCNs/Ti_3C_2	0.01-3.0	2000	2000	151.2	Ref 1
NHC_2-NH_3/Ar	0.01-2.5	200	1000	225.4	Ref 2
mesoporous graphitic carbon nanospring	0.01-2.0	2000	10000	99.9	Ref 3
commercial graphite	0.01-3.0	279	2000	255	Ref 4
Sulfur-grafted hollow carbon spheres	0.01-3.0	200	1000	250	Ref 5
S/N@C	0.01-2.0	2000	900	65	Ref 6
sulfur/nitrogen dual-doped hard carbon	0.01-3.0	100	500	234.5	Ref 7
carbon nanosheets	0.01-3.0	2000	1300	147	Ref 8
oxygen/fluorine dual-doped porous carbon	0.01-3.0	1000	2000	218	Ref 9
nitrogen-doped graphitic nanocarbons	0.01-2.0	200	200	189	Ref 10
nitrogen/oxygen codoped carbon hollow multihole bowls	0.01-2.5	1000	1000	133	Ref 11

N-doped amorphous carbon network	0.01-3.0	1000	4000	160	Ref 12
P-doped N-rich honeycomb-like carbon	0.01-3.0	1000	1000	270.4	Ref 13
nitrogen-doped hierarchical porous carbon	0.01-3.0	2000	12000	157	Ref 14
N-doped carbon nanofibers	0.01-3.0	2000	4000	146	Ref 15
Nitrogen/Oxygen Dual-Doped Hard Carbon	0.001-3.0	50	100	230.6	Ref 16
hierarchical carbon nanotube sponges	0.01-2.5	100	500	210	Ref 17
Sulfur/Oxygen Codoped Porous Hard Carbon Microspheres	0.01-2.5	1000	2000	108.4	Ref 18
wing-like porous carbon sheets	0.005-3.0	2000	3000	135	Ref 19
Sulphur-doped reduced graphene oxide	0.01-3.0	1000	500	229	Ref 20

References

[1] R. Zhao, H. Di, X. Hui, D. Zhao, R. Wang, C. Wang, L. Yin, *Energy & Environmental Science* **2020**.

[2] W. Yang, J. Zhou, S. Wang, W. Zhang, Z. Wang, F. Lv, K. Wang, Q. Sun, S. Guo, *Energy & Environmental Science* **2019**, *12*, 1605-1612.

[3] Y. Qian, S. Jiang, Y. Li, Z. Yi, J. Zhou, J. Tian, N. Lin, Y. Qian, *Angewandte Chemie* **2019**, *58*, 18108-18115.

[4] L. Fan, R. Ma, Q. Zhang, X. Jia, B. Lu, *Angewandte Chemie* **2019**, *58*, 10500-10505.

[5] J. Ding, H. Zhang, H. Zhou, J. Feng, X. Zheng, C. Zhong, E. Paek, W. Hu, D. Mitlin, *Adv Mater* **2019**, *31*, e1900429.

[6] A. Mahmood, S. Li, Z. Ali, H. Tabassum, B. Zhu, Z. Liang, W. Meng, W. Aftab, W. Guo, H. Zhang, M. Yousaf, S. Gao, R. Zou, Y. Zhao, *Adv Mater* **2019**, *31*, e1805430.
[7] Y. Liu, H. Dai, L. Wu, W. Zhou, L. He, W. Wang, W. Yan, Q. Huang, L. Fu, Y. Wu, *Advanced Energy Materials* **2019**, *9*, 1901379.
[8] J. T. Chen, B. J. Yang, H. J. Hou, H. X. Li, L. Liu, L. Zhang, X. B. Yan, *Advanced Energy Materials* **2019**, *9*, 1803894.
[9] J. Lu, C. Wang, H. Yu, S. Gong, G. Xia, P. Jiang, P. Xu, K. Yang, Q. Chen, *Advanced Functional Materials* **2019**, *29*, 1906126.
[10] W. L. Zhang, J. Ming, W. L. Zhao, X. C. Dong, M. N. Hedhili, P. M. F. J. Costa, H. N. Alshareef, *Advanced Functional Materials* **2019**, *29*, 1903641.
[11] Z. Zhang, B. Jia, L. Liu, Y. Zhao, H. Wu, M. Qin, K. Han, W. A. Wang, K. Xi, L. Zhang, G. Qi, X. Qu, R. V. Kumar, *ACS nano* **2019**, *13*, 11363-11371.
[12] J. F. Ruan, Y. H. Zhao, S. N. Luo, T. Yuan, J. H. Yang, D. L. Sun, S. Y. Zheng, *Energy Storage Materials* **2019**, *23*, 46-54.
[13] H. N. He, D. Huang, Y. G. Tang, Q. Wang, X. B. Ji, H. Y. Wang, Z. P. Guo, *Nano Energy* **2019**, *57*, 728-736.
[14] X. Zhou, L. Chen, W. Zhang, J. Wang, Z. Liu, S. Zeng, R. Xu, Y. Wu, S. Ye, Y. Feng, X. Cheng, Z. Peng, X. Li, Y. Yu, *Nano letters* **2019**, *19*, 4965-4973.
[15] Y. Xu, C. Zhang, M. Zhou, Q. Fu, C. Zhao, M. Wu, Y. Lei, *Nature communications* **2018**, *9*, 1720.
[16] J. Yang, Z. Ju, Y. Jiang, Z. Xing, B. Xi, J. Feng, S. Xiong, *Adv Mater* **2018**, *30*, 1700104.
[17] Y. Wang, Z. Wang, Y. Chen, H. Zhang, M. Yousaf, H. Wu, M. Zou, A. Cao, R. P. S. Han, *Adv Mater* **2018**, *30*, e1802074.
[18] M. Chen, W. Wang, X. Liang, S. Gong, J. Liu, Q. Wang, S. J. Guo, H. Yang, *Advanced Energy Materials* **2018**, *8*, 1800171.
[19] Y. Cui, W. Liu, X. Wang, J. Li, Y. Zhang, Y. Du, S. Liu, H. Wang, W. Feng, M. Chen, *ACS nano* **2019**, *13*, 11582-11592.
[20] J. L. Li, W. Qin, J. P. Xie, H. Lei, Y. Q. Zhu, W. Y. Huang, X. Xu, Z. J. Zhao, W. J. Mai, *Nano Energy* **2018**, *53*, 415-424.